

Multi-site modelling and reconstruction of past extreme skew surges along the French Atlantic coast

Nathan Huet¹, Philippe Naveau², Anne Sabourin³

¹DAIS, Università Ca' Foscari, Via Torino, 30170 Mestre, Venezia, Italy

²LSCE, UMR 8212, CEA-CNRS-UVSQ, IPSL & Université Paris-Saclay, Orme des Merisiers, 91190 Saint-Aubin, France

³MAP5, Université Paris Cité, CNRS, Rue des Saints-Pères, 75006 Paris, France

May 5, 2025

Abstract

Appropriate modelling of extreme skew surges is crucial, particularly for coastal risk management. Our study focuses on modelling extreme skew surges along the French Atlantic coast, with a particular emphasis on investigating the extremal dependence structure between stations. We employ the peak-over-threshold framework, where a multivariate extreme event is defined whenever at least one location records a large value, though not necessarily all stations simultaneously. A novel method for determining an appropriate level (threshold) above which observations can be classified as extreme is proposed. Two complementary approaches are explored. First, the multivariate generalized Pareto distribution is employed to model extremes, leveraging its properties to derive a generative model that predicts extreme skew surges at one station based on observed extremes at nearby stations. Second, a novel extreme regression framework is assessed for point predictions. This specific regression framework enables accurate point predictions using only the 'angle' of input variables, *i.e.*, input variables divided by their norms. The ultimate objective is to reconstruct historical skew surge time series at stations with limited data. This is achieved by integrating extreme skew surge data from stations with longer records, such as Brest and Saint-Nazaire, which provide over 150 years of observations.

1 Introduction

The rise in sea levels driven by global warming (Jevrejeva et al., 2016) increases the need to model and understand extreme sea level events, which can lead to devastating coastal flooding, such as the 1953 North Sea flood (McRobie et al., 2005). Assessing the intensity and frequency of these events is crucial for developing effective coastal risk management strategies aimed at reducing significant human and material losses (Genovese and Przymusiński, 2013; Chadenas et al., 2014; Karamouz et al., 2019). Classical studies on extreme sea levels often focus on past storm-induced floods and their impacts (Pineau-Guillou et al., 2012; Wadey et al., 2015), the influence of global warming and anthropogenic factors (Boumiz et al., 2023; Pan and Liu, 2020), forecasting and projections of extreme sea levels (Vousdoukas et al., 2018; Bellinghausen et al., 2024), and long-term historical data analysis to identify trends and estimate return periods of extreme events (Weisse et al., 2014; Tebaldi et al., 2021). We refer the reader to Bernier et al. (2024) for a recent comprehensive review on the topic of extreme sea levels (see also D'Arcy et al., 2023).

Aligned with the hydrological literature on extreme sea levels, this paper focuses on extreme surges¹. Sea levels can be decomposed into a deterministic tidal component and a stochastic non-tidal component called surges (Dixon and Tawn, 1994; Idier et al., 2012). Conversely, sea levels can be deduced from skew surges by convolution with predicted tides, namely by using the joint probability method (Pugh and Vassie, 1978, 1980) or its refinement (Tawn et al., 1989; Tawn, 1992).

In this work, our main environmental objective is to propose statistical methods to complete (reconstruct) coastal gauges recordings from other nearby stations that possess a much longer historical depth. To illustrate our approach, we will focus on tide gauges located along the French Atlantic coast. For example, the Brest station in Figure 1 spans a period going back to 1846, while the nearby station of Concarneau starts its recording in 1999. Although many of the cited references (see, e.g. Harter et al., 2024) consider the influence of covariates on extremes

¹A similar study on extreme sea levels is deferred to the Appendix.

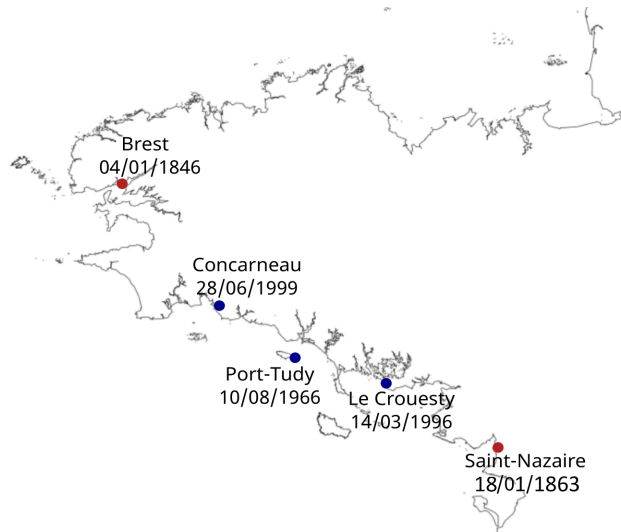


Figure 1: Five French tide gauge locations along the French Atlantic coast. Brest and Saint-Nazaire (red dots) have long sea level measurements, while Concarneau, Port Tudy and Le Crouesty (blue dots) have much shorter recordings. The objective of this work is to reconstruct missing surges in the past given extreme values from stations with long historical records (red dots).

at a given location, the literature is scarce regarding the task of reconstructing extreme events and their intensity within a multivariate extreme value modelling (see, e.g. Beck et al., 2020). One key element of the present work is to precisely model the statistical dependence among recorded extreme surges. To leverage multivariate extreme value theory in our task of completing extreme surges in short time series from long historical records at nearby stations, different regression models will be trained and compared on the overlapping record periods during which both older and newer tide gauges have been operational. The input stations are located at Brest and Saint-Nazaire, while the target stations for prediction are located at Port Tudy, Concarneau, and Le Crouesty. The reconstruction of extreme sea level time series (or equivalently extreme surge time series) is an active area of research aimed at producing increasingly precise inferences at specific sites and plays an important role in understanding ocean changes (see, e.g. Harter et al., 2024; Wang et al., 2024). Most studies in this domain, including those focused on forecasting (*i.e.*, predicting future values), use meteorological data, such as atmospheric pressure and wind, as predictors within various models, including multiple linear regression (Cid et al., 2018; Ji et al., 2020), random forests (Tadesse and Wahl, 2021) and deep learning (Bruneau et al., 2020; Tadesse et al., 2020). These approaches often disregard the potential spatial statistical dependence among locations. Univariate models are fitted at each site. Regional Frequency Analysis approaches (Hosking, 1997; Bardet et al., 2011; Bernardara et al., 2011; Collings et al., 2024) do leverage available information at nearby locations, however this information concerns the parameters of the aforementioned univariate distributions. To the best of our knowledge, the work which stands closest to ours (in the sense that spatial statistical dependence is used for reconstruction of extreme skew surges) is Calafat and Marcos (2020) who employ Bayesian hierarchical models to capture the dependence structure between extreme surges measured across Europe, for the purpose of climate reanalysis. Unlike their block-maxima approach, our work belongs within a peaks-over-threshold framework. In addition to proposing a different fully parametric model, we also introduce a nonparametric machine-learning-based method to reduce reliance on strict model assumptions.

The main methodological purpose of this work is to promote the use of two new approaches derived from the theory of multivariate extreme values for the analysis of extreme sea levels in geoscience and climate research (see, e.g. Naveau and Segers, 2025, for a recent review on multivariate extremes). On the one hand, we propose a machine learning approach designed to minimize a pointwise prediction performance criterion. On the other hand, we implement a parametric modelling approach that enables comprehensive (conditional) distributional modelling of the missing component, providing prediction confidence intervals. We carefully highlight the theoretical connections between the two approaches, emphasizing that, despite their methodological differences, the statistical assumptions regarding the distributional tail of the data are essentially equivalent. To the best of our knowledge, such comparisons between machine learning and parametric approaches are rare in the applied statistical literature dedicated to multivariate extreme analysis. In particular, sections 3 and 4 explain the fundamental relationships between these two approaches that may seem incompatible at first view. Another contribution lies in proposing

a simple and original method for determining an appropriate level (threshold) above which observations can be classified as extreme.

The nonparametric machine learning method envisioned here is closely related to an active area of research focused on developing a sound statistical learning and machine learning framework for multivariate extreme value settings, relying on minimal model assumptions. Examples include clustering methods (Goix et al., 2016, 2017; Chiapino et al., 2019; Simpson et al., 2020; Meyer and Wintenberger, 2021; Janßen and Wan, 2020; Vignotto et al., 2021; Meyer and Wintenberger, 2023), principal component analysis (Cooley and Thibaud, 2019; Drees and Sabourin, 2021; Cléménçon et al., 2024), graphical models (Engelke and Hitz, 2020), classification (Jalalzai et al., 2018). These machine learning algorithms dedicated to extreme value analysis are not black boxes; the understanding of statistical learning mechanisms and error margins is rapidly advancing, as seen in the recent review Cléménçon and Sabourin (2025). In this work, we employ the least-squares regression procedure proposed in Huet et al. (2023), designed for extreme-value predictive problems where extremality is assessed relative to covariates. In our case, the covariates are surges recorded at neighbouring stations. The regression algorithm generates a predictive function that enables the estimation of surges at the target station, given the covariate, particularly when the norm of the covariate is large.

The parametric method implemented here leverages recent advances in parametric multivariate extreme value modelling. Specifically, we use the flexible multivariate generalized Pareto model developed in Kiriliouk et al. (2019); Rootzén et al. (2018); Rootzén et al. (2018), building on earlier work from Rootzén and Tajvidi (2006). In applications, this framework has proved relevant for different purposes, such as the joint simulation of extreme waves (Legrand et al., 2023), anomaly detection of extreme precipitation (Nezaki and Nagatsuka, 2023), and risk modelling associated with wildfires (Cisneros et al., 2024). In this framework, an observation is considered extreme if at least one of its input components exceeds a critical threshold (see Section 3). This definition is well-suited to the present use case, as a single large skew surge can lead to flooding at the target station, regardless of conditions at neighbouring stations. With the addition of parametric assumptions, model fitting enables comprehensive modelling of the full conditional distribution of the skew surges at the target station, given large values at one of the ‘covariate’ stations.

Note that, in this work, the terms *parametric* and *nonparametric* only characterize the multivariate dependence structure, but not the marginal behaviours. At the marginal level, extreme value theory provides a strong justification for parametric models for exceedances. In contrast, asymptotic mathematical arguments point towards a non-parametric dependence structure for multivariate extremes (see, e.g. Naveau and Segers, 2025). Still, parametric dependence family choices are often made for convenience and interpretation purposes. In addition, they facilitate the construction of confidence intervals.

This paper is structured as follows. In Section 2, we present the skew surge data. Section 3 introduces the theoretical framework necessary to understand the proposed methods. In Section 4, we outline the marginal preprocessing and threshold selection, followed by two prediction schemes, which are described using two algorithms. The results of applying these procedures to the skew surge datasets are presented in Section 5. Additional details are deferred to the Appendix, in particular, additional analyses conducted on sea levels and two other output stations are provided in Section D.

2 Skew surge time series

The dataset considered in our work is produced by the REFMAR (Réseaux de REFérence des observations MARégraphiques), a sea level observation network managed by the SHOM (Service Hydrographique et Océanographique de la Marine). Some tide gauges in the observation network have recorded over a century of hourly measurements, while others have only been operational for about twenty years. Figure 1 shows the locations of the five tide gauges involved in our study, along with the dates of their first recordings. To avoid modelling tide-surge interactions in this dataset, which is beyond the scope of this study, we only focus on skew surges which are defined as the difference between the maximum observed sea level and the astronomically predicted tide. Skew surges have been shown to be independent of high tides (Williams et al., 2016). This independence has been empirically validated for most tide gauges along the French coast, including the five stations considered in this study (Kergadallan et al., 2014; Kergadallan, 2022).

As mentioned in the introduction, the analysis focuses on the analysis of maximum skew surges observed during tides along the French Atlantic coast. The dataset comprises hourly validated records, each associated with a timestamp, from 11/08/1966 to 31/12/2023. The input measurements are provided by the long-range tide gauges located at Brest and Saint-Nazaire, while the output stations with limited historical records are located at Port Tudy, Concarneau, and Le Crouesty (see Figure 1). Three separate studies are conducted, each aimed at predicting

values as one output station. The analysis with output skew surges measured at Port Tudy is presented in the main text, while the analyses for sea levels and the other two stations are deferred to Section D of the Appendix, as similar conclusions apply across all three stations.

In the sequel, the notation Y stands for the response (target) variable, while \mathbf{X} is the covariate vector. Here, $\mathbf{X} = (X_B, X_N)^T$ represents the bivariate vector comprising skew surges at the Brest and Saint-Nazaire stations, while Y represents skew surges at an output station.

To evaluate the performance of our methods, each dataset is divided into two subsets. The marginal and joint dependence structures are learnt on the training set, comprising the most recent observations, while the model performances are evaluated on the test set, consisting of the earliest observations. The training and test sets are divided on December 31, 1999, for Port Tudy, in 2010 for Concarneau, and in 2014 for Le Crouesty, ensuring similar sizes across the sets.

In practice, the marginal observations at the output station are unknown; thus, an observation is considered extreme if at least one of the values from the two input stations exceeds a large threshold. To reduce computational costs and because we focus on extremes, we discard measurements where both X_B and X_N fall below their empirical medians. Additionally, for convenience, we shift the origin so that the componentwise minimum value of the selected measurements is zero (see Section A in the Appendix for details). These operations on the training set yield the observations displayed in Figure 2.

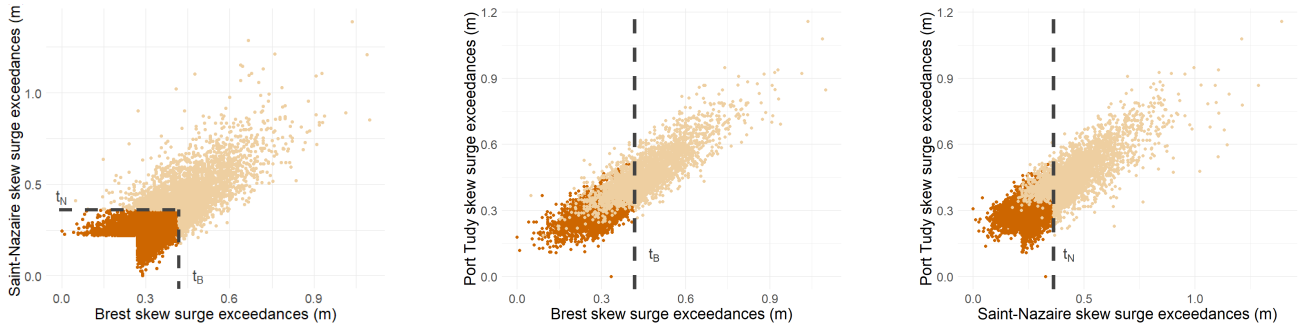


Figure 2: Pairwise skew surge exceedances for all pairs of stations from 01/12/2000 to 31/12/2023. Dark orange (resp. light orange) points represent the observations below (resp. above) the threshold specified in Table 1. The grey dotted lines represent the chosen marginal thresholds via Algorithm 1 (see Section 5.1).

3 Marginal and multivariate modeling of extremes: Background

Multivariate extreme value models are asymptotically justified under mild regularity assumptions regarding their tail behavior. These assumptions imply that after some marginal standardization, the joint distribution enjoys a homogeneity property in the tails, making extrapolation possible. This section provides some minimal background in univariate and multivariate Extreme Value Theory (EVT) underlying the methods developed in the following sections. Here and throughout, multivariate objects are denoted in bold font to avoid confusion, *e.g.* $\mathbf{z} = (z_1, \dots, z_{d+1})^T \in \mathbb{R}^{d+1}$. To simplify notations, for $\mathbf{x} \in \mathbb{R}^d$ and $y \in \mathbb{R}$, we will write expressions like $(\mathbf{x}^T, y)^T \in \mathbb{R}^{d+1}$ more concisely as $(\mathbf{x}, y) \in \mathbb{R}^{d+1}$. Let $\mathbf{Z} = (\mathbf{X}, Y) \in \mathbb{R}^{d+1}$ represent the considered random pair (covariate, target), with $\mathbf{X} \in \mathbb{R}^d$ and $Y \in \mathbb{R}$ and let F_j , for $1 \leq j \leq d+1$, denote the j^{th} marginal distribution of the random vector \mathbf{Z} , $F_j(z) = \mathbb{P}(Z_j \leq z)$. Univariate operations applied to multivariate objects should be understood componentwise, *i.e.*, for $f_\theta : \mathbb{R} \rightarrow \mathbb{R}$, $\theta \in \mathbb{R}^d$ and $\mathbf{x} \in \mathbb{R}^d$, $f_\theta(\mathbf{x}) = (f_{\theta_1}(x_1), \dots, f_{\theta_d}(x_d))$. The order relations $\leq, <$ in \mathbb{R}^d should be understood as the partial order resulting from componentwise comparisons, *i.e.* for $\mathbf{x}, \mathbf{t} \in \mathbb{R}^d$, say, where \mathbf{t} typically represents a multivariate high threshold for the covariate \mathbf{X} , the notation $\mathbf{x} \leq \mathbf{t}$ means that for *all* $1 \leq j \leq d$, $x_j \leq t_j$, while $\mathbf{x} \not\leq \mathbf{t}$ means that for *some* $1 \leq j \leq d$, $x_j > t_j$. We denote by $\mathcal{L}(T)$ the distribution of a random element T and $\mathcal{L}(T_n) \rightarrow \mathcal{L}(T)$ means that the random variables or vectors T_n converge in distribution to T .

3.1 Marginal models for extremes

A key result in dimension one (Balkema and De Haan, 1974) is that under mild assumptions, the distribution of excesses above high thresholds may be legitimately modelled by a Generalized Pareto (GP) distribution $H_{\sigma, \xi}(z) = 1 - (1 + \xi z/\sigma)_+^{-1/\xi}$, *i.e.*, an asymptotically valid approximation of $(1 - F_j(z + t_j))/(1 - F_j(t_j))$ is $1 - H_{\sigma_j, \xi_j}(z)$

where t_j is a large threshold and ξ_j, σ_j are respectively a shape and a scale parameter for the j^{th} margin. However, modelling excesses above high thresholds by a GP distribution has some limitations. First, a pervasive challenge in extreme value analysis is selecting an appropriate threshold above which observations are considered extreme, so that the GP distribution is in effect an appropriate model for excesses. Second, certain extreme-value frameworks necessitate modelling the entire distribution, not just the tail above a threshold. Indeed, as mentioned in Section 2, an observation is considered extreme if a large value is recorded at least at one of the input stations. Therefore, marginal observations of multivariate records considered as extreme may include non-extreme components (e.g., a storm affecting only Saint-Nazaire but not Brest). These residual non-extreme observations fall into the left tail of the marginal distribution at each station (see Figure 3).

In this paper, in order to avoid imposing (or having to make a choice for) a threshold t_j , we consider a flexible parametric family, the Extended Generalized Pareto (EGP) distribution (Papastathopoulos and Tawn, 2013; Naveau et al., 2016), which permits to model the entire positive part of the marginal distribution, while the conditional distribution of excesses above high threshold is asymptotically equivalent to a GP distribution. This modelling strategy has been applied for modelling extreme precipitation (Tencaliec et al., 2020; Rivoire et al., 2021; Nanditha et al., 2024), large wave heights (Legrand et al., 2023) or strong wind speed (Turkman et al., 2021). Specifically, we use the simplest EGP model (EGPD3 in Papastathopoulos and Tawn (2013)), with distribution function

$$F_{\sigma, \xi, \kappa}(z) = \left(1 - \left(1 + \frac{\xi z}{\sigma}\right)^{-1/\xi}\right)^\kappa, \quad (3.1)$$

where $\sigma > 0$ is a scale parameter, $\xi \in \mathbb{R}$ is a shape parameter and $\kappa > 0$ is a lower tail shape parameter. Indeed $F_{\sigma, \xi, \kappa}(z) \approx Cst \times z^\kappa$, as $z \rightarrow 0$. The associated density function $f_{\sigma, \xi, \kappa}$ is

$$f_{\sigma, \xi, \kappa}(z) = \frac{\kappa}{\sigma} \left(1 + \frac{\xi z}{\sigma}\right)^{-1/\xi - 1} \left(1 - \left(1 + \frac{\xi z}{\sigma}\right)^{-1/\xi}\right)^{\kappa - 1}. \quad (3.2)$$

The EGP distribution has support $[0, +\infty[$ if $\xi \geq 0$ and $[0, -\sigma/\xi]$ if $\xi < 0$.

3.2 Multivariate modelling of extremes

As a multivariate extension of the univariate framework introduced above, an essential result is that for a large class of distributions, including e.g. multivariate Gaussian, Cauchy or Student multivariate families, the joint distribution of properly rescaled excesses above high thresholds converges to a Multivariate Generalized Pareto (MGP) distribution (Rootzén and Tajvidi, 2006; Rootzén et al., 2018; Rootzén et al., 2018; Kiriliouk et al., 2019). In practice, this implies that for a sufficiently high multivariate threshold $\mathbf{t} = (t_1, \dots, t_{d+1})$,

$$\mathcal{L}((\mathbf{Z} - \mathbf{t}) \vee \boldsymbol{\eta} \mid \mathbf{Z} \not\leq \mathbf{t}) \approx \mathcal{L}(\mathbf{Z}_\infty), \quad (3.3)$$

where \mathbf{Z}_∞ is a MGP random vector and $\boldsymbol{\eta}$ is the vector of lower end-points of marginal distributions of \mathbf{Z}_∞ . The latter marginal distributions are, by construction, univariate GP distributions above zero, namely

$$\mathbb{P}(Z_{\infty, j} \geq z \mid Z_{\infty, j} > 0) = 1 - H_{\sigma_j, \xi_j}(z) := \left(1 + \frac{\xi_j}{\sigma_j} z\right)_+^{-1/\xi_j}.$$

For modelling purposes a customary approach is to consider marginally standardized versions of \mathbf{Z} . This allows for convenient representations of the limit distribution amenable both to parametric modelling and statistical learning algorithms. Standard statistical practice in multivariate EVT involves modelling separately the tails of the marginal distributions F_j and the extremal dependence structure encapsulated by the limiting distribution of marginally standardized excesses conditioned on an excess above high (multivariate) thresholds. Of course, different marginalisation choices lead to different limit models and statistical methods, which are asymptotically equivalent after back-transformation to the original scale. The two methods implemented and compared in this work (*resp.* a non parametric regression algorithm and a parametric model) are respectively formulated with unit Pareto margins, and unit Exponential margins, introduced next.

3.2.1 Pareto margins modelling

Consider the componentwise transformation

$$p(z) = \left(\frac{1}{1 - F_1(z_1)}, \dots, \frac{1}{1 - F_{d+1}(z_{d+1})}\right)^T \quad (3.4)$$

and let $p(\mathbf{Z})$ denote the marginally transformed random observation. Because the marginal distributions are unknown, a preliminary step is to fit marginal models to each margin Z_j , as outlined in the previous paragraph. Then, choosing any norm $\|\cdot\|$ on \mathbb{R}^{d+1} , and switching to pseudo-polar coordinates by letting $\Theta = \|p(\mathbf{Z})\|^{-1}p(\mathbf{Z})$, (3.3) implies in particular that

$$\mathcal{L}(\|p(\mathbf{Z})\|/t, \Theta \mid \|p(\mathbf{Z})\| > t) \rightarrow \mathcal{L}(R_\infty, \Theta_\infty), \quad (3.5)$$

as $t \rightarrow +\infty$, where R_∞ is a radial component, Θ_∞ is a pseudo-angle, and R_∞ and Θ_∞ are independent. An equivalent writing of (3.5) is that

$$\mathcal{L}(t^{-1}p(\mathbf{Z}) \mid \|p(\mathbf{Z})\| > t) \rightarrow \mathcal{L}(\tilde{\mathbf{Z}}_\infty), \quad (3.6)$$

as $t \rightarrow +\infty$, where $\tilde{\mathbf{Z}}_\infty$ has a multiplicative structure $\tilde{\mathbf{Z}}_\infty = R_\infty \cdot \Theta_\infty$ with independent factors R_∞, Θ_∞ as in (3.5). In practice, a wealth of statistical analyses of extreme environmental events have been successfully conducted based on that assumption (Davison and Huser, 2015). The reader may refer to Resnick (2008) for a comprehensive presentation of multivariate EVT and its connections with Condition (3.5).

3.2.2 Exponential margins in the multivariate generalized Pareto model

As an alternative to the Pareto scaling depicted in the previous paragraph, recent advances in statistical modelling of multivariate extremes (Rootzén and Tajvidi, 2006; Rootzén et al., 2018; Rootzén et al., 2018; Kiriliouk et al., 2019) have revealed convenient limiting structures on the exponential scale, in the MGP distribution introduced at the beginning of this section. Observe first that if $p(Z_j)$ follows a unit Pareto distribution then $\log(p(Z_j))$ follows a unit exponential distribution. Also by construction, the logarithm function turns multiplicative structures into additive structures. More precisely, for $\mathbf{z} \in \mathbb{R}^{d+1}$, let

$$e(\mathbf{z}) = (-\log(1 - F_1(z_1)), \dots, -\log(1 - F_{d+1}(z_{d+1})))^T = \log \circ p(\mathbf{z}) \quad (3.7)$$

denote a componentwise transformation mapping a random vector with margins F_j to a vector with exponential margins, and define accordingly a marginally transformed vector

$$e(\mathbf{Z}) = (\log(p(Z_1)), \dots, \log(p(Z_{d+1})))^T.$$

Then under the same assumptions as the ones underlying the multivariate tail model for $p(\mathbf{Z})$ with Pareto margins, namely (3.3), considering a multivariate threshold \mathbf{t}' tending to infinity,

$$\mathcal{L}(e(\mathbf{Z}) - \mathbf{t}' \mid e(\mathbf{Z}) \preceq \mathbf{t}') \rightarrow \mathcal{L}(\mathbf{Z}'_\infty), \quad (3.8)$$

where the margins of $\tilde{\mathbf{Z}}_\infty$, when conditioned on being positive, follow a unit exponential distribution,

$$\mathbb{P}(Z'_{\infty,j} \geq z \mid Z'_{\infty,j} > 0) = \exp(-z), \quad 1 \leq j \leq d+1.$$

The random vector \mathbf{Z}'_∞ is called a *standard* MGP distribution (Rootzén et al., 2018; Wan, 2024). As hinted above, the multiplicative structure of $\tilde{\mathbf{Z}}_\infty$ in (3.6) translates into an additional structure for \mathbf{Z}'_∞ in (3.8),

$$\mathbf{Z}'_\infty = E + \mathbf{T} - \max \mathbf{T}, \quad (3.9)$$

where $E \in \mathbb{R}$ is a unit exponential random variable and \mathbf{T} is a random vector valued in \mathbb{R}^{d+1} , independent of E . Conversely, any random vector \mathbf{T} in \mathbb{R}^{d+1} gives rise to a standard MGP vector \mathbf{Z}'_∞ through (3.9). The additive structure (3.9) permits to construct flexible models for \mathbf{Z}'_∞ (after transformation to exponential margins) amenable to likelihood inference, based on any parametric model for \mathbf{T} (see Appendix C.1 for more details).

4 Prediction of a missing component: Methodology

This section presents a detailed description of the methodologies developed and implemented in this study to predict the target Y based on observations of a covariate \mathbf{X} exceeding a sufficiently large multivariate threshold \mathbf{t}_X , using training data where both the covariate and the target are recorded simultaneously. We denote the training dataset by $\mathcal{D}_n = \{\mathbf{Z}_i\}_{1 \leq i \leq n} = \{(\mathbf{X}_i, Y_i)\}_{1 \leq i \leq n}$. Recall from the Introduction that \mathcal{D}_n results from a pre-processing step fully described in Appendix A. Following the framework outlined in Section 3, Sections 4.1, 4.2, and 4.3 respectively detail our methodologies for univariate analysis, point prediction of a missing component using a Machine Learning algorithm, and distribution regression through parametric modelling and likelihood-based inference of the conditional distribution of a missing component.

Algorithm 1 Marginal modeling and threshold selection.

INPUT: Training dataset $\{X_1, \dots, X_n\}$ with $X_i \in \mathbb{R}$ for all $1 \leq i \leq n$.

Marginal Fitting: Fit an EGP distribution to the dataset to obtain a triplet of estimated parameters $(\sigma, \xi, \kappa) \in [0, +\infty[\times \mathbb{R} \times [0, +\infty[$.

Threshold computation: Compute the threshold t according to the EGP estimated terms

$$t = \frac{\sigma}{\xi} \left(\left(\frac{4\xi^2 + 3(\kappa\xi + \kappa + \xi) - 1 - \sqrt{(4\xi^2 + 3(\kappa\xi + \kappa + \xi) - 1)^2 - 4(\kappa^2 + 2\xi^2 + 3\kappa\xi)(2\xi^2 + 3\xi + 1)}}{2(\kappa^2 + 2\xi^2 + 3\kappa\xi)} \right)^{-\xi} - 1 \right).$$

OUTPUT: estimated marginal EGP parameters (σ, ξ, κ) and a threshold t .

4.1 Univariate study and threshold selection

As outlined in Section 3.1, we model the marginal distributions by fitting an EGP model (3.1) to each coordinate of the full training dataset \mathcal{D}_n . As illustrated in Section 5 this specific marginal model fits the considered data set reasonably well (see Figure 3). Note that alternative variants of the chosen EGP submodel, such as the EGP family introduced in Naveau et al. (2016), could have been considered. Another possible approach would be to use the traditional method of modelling with a GP distribution above a preselected threshold and the empirical cdf below threshold as discussed in *e.g.*, Heffernan and Tawn (2004). Since marginal modelling is not the central focus of our work (our primary emphasis being on multivariate modelling), we do not provide a detailed comparison of all potential univariate modelling approaches.

The necessary step of univariate modelling, classically aimed at performing marginal transformations in (3.4) and (3.7), also enables us to select a multivariate threshold \mathbf{t} in (3.3) which, in the multivariate analysis, allows for the identification of extreme training data. To the best of our knowledge, the method we propose here and below for threshold selection is novel. As noted in Naveau et al. (2016) (see also Section 3.1), the EGP distribution behaves similarly to a GP distribution in the right tail. Since the GP density is strictly convex for $\xi > -1/2$ (a condition always met here, see Table 1), the EGP density $f_{\sigma, \xi, \kappa}$ (3.2) is also strictly convex for sufficiently large values and closely resembles a GP distribution on this domain. This suggests to choose the threshold as the lowest value above which the fitted EGP density is convex. Numerically, this is the largest zero of the second derivative $\frac{d^2 f_{\sigma, \xi, \kappa}(z)}{dz^2}$. Straightforward computations reported in Appendix B yield an explicit expression for the latter value which is given in Algorithm 1. The advantage of this automatic selection procedure is that it eliminates reliance on visual inspection of stability plots as discussed in Kiriliouk et al. (2019); Legrand et al. (2023); Huet et al. (2023), which can sometimes be challenging to interpret, thereby reducing a layer of arbitrariness. The relevance of this approach is illustrated in Section 5, namely Figure 6 shows that the EGP and GP distributions are indeed close to indistinguishable above the chosen threshold.

In the sequel, we denote by $\boldsymbol{\sigma}, \boldsymbol{\xi}, \boldsymbol{\kappa} = (\boldsymbol{\sigma}_X, \boldsymbol{\sigma}_Y), (\boldsymbol{\xi}_X, \boldsymbol{\xi}_Y), (\boldsymbol{\kappa}_X, \boldsymbol{\kappa}_Y) \in \mathbb{R}^{d+1}$, with $\boldsymbol{\sigma}_X = (\sigma_1, \dots, \sigma_d)^T$, $\boldsymbol{\xi}_X = (\xi_1, \dots, \xi_d)^T$, $\boldsymbol{\kappa}_X = (\kappa_1, \dots, \kappa_d)^T \in \mathbb{R}^d$ the EGP parameters, and $\mathbf{t} = (t_X, t_Y) \in \mathbb{R}^{d+1}$, with $t_X = (t_1, \dots, t_d)^T \in \mathbb{R}^d$, the multivariate extreme threshold, resulting from Algorithm 1 applied independently to each marginal dataset $\{Z_{i,j}\}_{1 \leq i \leq n}$, for $1 \leq j \leq d+1$. The latter threshold \mathbf{t} allows to define a subset of extreme observations \mathcal{D}_{ext} for subsequent multivariate analysis, in terms of an excess of \mathbf{t} in at least one component of the covariable. We let k denote the number of such extreme training observations and without loss of generality (up to reordering the indices), to alleviate notations, we assume that these extreme observations form the first k entries of the training set, namely

$$\mathcal{D}_{ext} = \{\mathbf{Z}_i = (\mathbf{X}_i, Y_i), \text{ such that } \mathbf{X}_i \not\leq \mathbf{t}_X\}_{1 \leq i \leq n} = \{\mathbf{Z}_i\}_{1 \leq i \leq k}.$$

4.2 Point prediction based on Machine Learning

The marginal modelling step from Section 3.1 is crucially exploited both for estimating the marginal distributions F_j involved in (3.4) and for threshold selection in (3.3) via Algorithm 1. In the sequel for clarity we denote by $p_{\sigma, \xi, \kappa}$ the marginal transformation based on EGP-modelled marginals $F_{\sigma, \xi, \kappa}$,

$$p_{\sigma, \xi, \kappa}(x) = \frac{1}{1 - F_{\sigma, \xi, \kappa}(x)}, \quad (4.1)$$

and we use boldface notation for the multivariate mapping $p_{\boldsymbol{\sigma}, \boldsymbol{\xi}, \boldsymbol{\kappa}}(\mathbf{z}) = (p_{\boldsymbol{\sigma}_X, \boldsymbol{\xi}_X, \boldsymbol{\kappa}_X}((z_1, \dots, z_d)), p_{\boldsymbol{\sigma}_Y, \boldsymbol{\xi}_Y, \boldsymbol{\kappa}_Y}(z_{d+1}))$ so that $p_{\boldsymbol{\sigma}, \boldsymbol{\xi}, \boldsymbol{\kappa}}(\mathbf{Z})$ is the Pareto-transformed variable, where $\boldsymbol{\sigma}, \boldsymbol{\xi}, \boldsymbol{\kappa} = (\boldsymbol{\sigma}_X, \boldsymbol{\sigma}_Y), (\boldsymbol{\xi}_X, \boldsymbol{\xi}_Y), (\boldsymbol{\kappa}_X, \boldsymbol{\kappa}_Y)$ are the parameters

estimated with Algorithm 1. For conciseness, and when clear from the context, we denote $p_{\sigma_X, \xi_X, \kappa_X}$, $p_{\sigma_Y, \xi_Y, \kappa_Y}$ and $p_{\sigma, \xi, \kappa}$ simply as p . Note that the former always applies to a quantity homogeneous to \mathbf{X} , the second to a quantity homogeneous to Y , and the latter to a quantity homogeneous to \mathbf{Z} .

Getting back to the prediction task considered in this paper, recall that the goal is to predict $Y = Z_{d+1}$ based on $\mathbf{X} = (Z_1, \dots, Z_d)^T$. This may be done by predicting $p(Y)$ based on $p(\mathbf{X})$ and then transforming back the predicted value for $p(Y)$ through an inversion of (3.4).

For mathematical reasons rooted in statistical learning theory, prediction tasks associated with bounded target variables are more convenient to handle. The intuition behind is that boundedness prevents spurious behaviours of the least square estimator arising with large residuals. With this in mind, following in the footsteps of Huet et al. (2023) (Example 2 in the cited reference), our strategy here is to learn a regression function \hat{f} to predict an intermediate, bounded, 'angular' target

$$\Theta_Y = p(Y)/\|p(\mathbf{Z})\|, \quad (4.2)$$

using any off-the-shelf machine learning algorithm trained on the extreme dataset \mathcal{D}_{ext} . The learnt regression function \hat{f} for Θ_Y then allows to define a prediction function \hat{g} for the original target Y by plugging the predicted value $\hat{\Theta}_Y = \hat{f}(\mathbf{X})$ into the straightforward inversion of the above display (with $\|\cdot\|$ chosen as the Euclidean norm)

$$p(Y) = \Theta_Y \|p(\mathbf{X})\| / \sqrt{(1 - \Theta_Y^2)},$$

In the end, the target quantity Y is obtained by transforming back to the natural marginal scale using an inversion $p_{\sigma_Y, \xi_Y, \kappa_Y}^{-1}$ of (4.1). Summarizing, the final prediction function \hat{g} makes predictions \hat{Y} defined by

$$\hat{Y} = \hat{g}(\mathbf{X}) = p_{\sigma_Y, \xi_Y, \kappa_Y}^{-1} \left(\hat{f}(\mathbf{X}) \|p(\mathbf{X})\| / \sqrt{(1 - \hat{f}(\mathbf{X})^2)} \right).$$

Regarding the training step aiming at constructing \hat{f} to predict Θ_Y as described above, a key finding in Huet et al. (2023) is that it is advisable to leverage an independence property, above high thresholds, regarding angular and radial components of the rescaled pair (covariate, target) (see (3.5)). More precisely, under mild additional regularity assumptions regarding the density functions (See Example 2 of Huet et al. (2023) for details), letting $\Theta_X = \|p(\mathbf{X})\|^{-1} p(\mathbf{X})$, and defining Θ_Y as in (4.2), it holds that

$$\mathcal{L} \left((\|p(\mathbf{X})\|/t, \Theta_X, \Theta_Y) \mid \|p(\mathbf{X})\| > t \right) \xrightarrow[t \rightarrow +\infty]{} \mathcal{L}(\|\tilde{\mathbf{X}}_\infty\|, \Theta_{X,\infty}, \Theta_{Y,\infty}),$$

where $\tilde{\mathbf{X}}_\infty = \|\tilde{\mathbf{X}}_\infty\| \Theta_{X,\infty}$ is the limit in distribution of $\mathcal{L}(t^{-1} p(\mathbf{X}) \mid \|p(\mathbf{X})\| > t)$ as $t \rightarrow +\infty$. Importantly, in the right-hand side of the above display, the radial component $\|\tilde{\mathbf{X}}_\infty\|$ is independent of the angular components $(\Theta_{X,\infty}, \Theta_{Y,\infty})$. This suggests learning a prediction function for Θ_Y (conditional on $\|p(\mathbf{X})\|$ being large) taking as input only the *angular* component Θ_X of the largest observations, not their radial component $\|p(\mathbf{X})\|$. This strategy is embodied in the ROXANE Algorithm 2, originally proposed by Huet et al. (2023). ROXANE permits to learn a prediction function $\hat{f}(\mathbf{X}) := \hat{f}_\Theta(\Theta_X)$ that depends only on the angular part Θ_X of \mathbf{X} and is asymptotically optimal in terms of mean squared error. In practice, ROXANE should be viewed as a meta-algorithm which may be implemented with any machine learning prediction algorithm \mathcal{A}_{pred} , suitable for prediction of a real-valued, continuous target. The algorithm \mathcal{A}_{pred} is trained on the (covariate, target) pairs $(\Theta_{X,i}, \Theta_{Y,i})$, which are obtained by applying the previously described transformations to the extreme observations $\mathbf{Z}_i \in \mathcal{D}_{ext}$. The uniqueness of ROXANE lies in the pre-processing and rescaling steps described above. In our experiments (Section 5), we present results obtained using two specific algorithms \mathcal{A}_{pred} , namely Ordinary Least Squares (OLS) and Random Forest (RF), although other choices for the algorithm \mathcal{A}_{pred} would have been equally valid. It is rigorously demonstrated in Huet et al. (2023) that ROXANE enjoys strong statistical guarantees when implemented with a stylized example of a prediction machine learning algorithm, namely a least squares algorithm searching for a minimizer of the squared error over a class of predictors with controlled complexity, with arguments pertaining to Vapnik-Chervonenkis theory and concentration inequalities.

Numerically, the authors perform experiments on a toy example using financial data, where (multivariate) extreme value theory is generally recognized as providing suitable tail models. To our best knowledge the practical performance of ROXANE on environmental data such as skew surge time series has never been investigated. In particular, no comparative study has yet been conducted between this model-agnostic method and parametric modelling approaches, such as the one proposed in the next section.

Algorithm 2 ROXANE regression algorithm.

TRAINING STEP

INPUT:

- The output of Algorithm 1 applied independently to each marginal dataset $\{Z_{i,j}\}_{1 \leq i \leq n}$ for $1 \leq j \leq d+1$: EGP parameters $\boldsymbol{\sigma}, \boldsymbol{\xi}, \boldsymbol{\kappa} = (\boldsymbol{\sigma}_X, \boldsymbol{\sigma}_Y), (\boldsymbol{\xi}_X, \boldsymbol{\xi}_Y), (\boldsymbol{\kappa}_X, \boldsymbol{\kappa}_Y) \in \mathbb{R}^{d+1}$; A multivariate threshold $\mathbf{t}_X \in \mathbb{R}^d$ for the covariate; Extreme training dataset made of observations such that $\mathbf{X} \not\leq \mathbf{t}_X$, $\mathcal{D}_{ext} = \{\mathbf{Z}_1, \dots, \mathbf{Z}_k\}$ where $\mathbf{Z}_i = (\mathbf{X}_i, Y_i) \in \mathbb{R}^{d+1}$ represents a covariate-target pair.
- A machine learning algorithm \mathcal{A}_{pred} suitable for prediction of a real target (*e.g.* least squares, random forest, support vector regression, k-nn, gradient boosting, neural networks,...

Extreme data transformation to Pareto margins and angular rescaling: Apply the componentwise Pareto transformation (4.1) to extreme observations

$$p_{\boldsymbol{\sigma}, \boldsymbol{\xi}, \boldsymbol{\kappa}}(\mathbf{Z}_i) = (p_{\boldsymbol{\sigma}_X, \boldsymbol{\xi}_X, \boldsymbol{\kappa}_X}(\mathbf{X}_i), p_{\boldsymbol{\sigma}_Y, \boldsymbol{\xi}_Y, \boldsymbol{\kappa}_Y}(Y_i)), \quad \text{for } 1 \leq i \leq k \text{ (equivalently for } \mathbf{Z}_i \in \mathcal{D}_{ext}).$$

Form the angular components of the covariates and the target,

$$\Theta_{X,i} = \|p_{\boldsymbol{\sigma}_X, \boldsymbol{\xi}_X, \boldsymbol{\kappa}_X}(\mathbf{X}_i)\|^{-1} p_{\boldsymbol{\sigma}_X, \boldsymbol{\xi}_X, \boldsymbol{\kappa}_X}(\mathbf{X}_i), \quad \Theta_{Y,i} = p_{\boldsymbol{\sigma}_Y, \boldsymbol{\xi}_Y, \boldsymbol{\kappa}_Y}(Y_i) / \|p_{\boldsymbol{\sigma}, \boldsymbol{\xi}, \boldsymbol{\kappa}}(\mathbf{Z}_i)\|.$$

Training the angular prediction model: Train Algorithm \mathcal{A}_{pred} on the angular training dataset \mathcal{D}_{ang} made of angular pairs (covariates, target)

$$\mathcal{D}_{ang} = \{\Theta_{X,i}, \Theta_{Y,i}\}_{1 \leq i \leq k}.$$

Intermediate output: An angular prediction function \hat{f}_Θ , and an associated prediction function \hat{f} : For a new (test) extreme covariate \mathbf{x} such that $\mathbf{x} \not\leq \mathbf{t}_X$, the prediction of \mathcal{A}_{pred} regarding $\Theta_y = y / \|(x, y)\|$ is

$$\hat{f}(\mathbf{x}) = \hat{f}_\Theta(\Theta_{\mathbf{x}}),$$

where $\Theta_{\mathbf{x}} = p_{\boldsymbol{\sigma}_X, \boldsymbol{\xi}_X, \boldsymbol{\kappa}_X}(\mathbf{x}) / \|p_{\boldsymbol{\sigma}_X, \boldsymbol{\xi}_X, \boldsymbol{\kappa}_X}(\mathbf{x})\|$.

OUTPUT of the training step: A prediction function \hat{g} defined for $\mathbf{x} \not\leq \mathbf{t}_X$,

$$\hat{g}(\mathbf{x}) = p_{\boldsymbol{\sigma}_Y, \boldsymbol{\xi}_Y, \boldsymbol{\kappa}_Y}^{-1} \left(\hat{f}(\mathbf{x}) \|p_{\boldsymbol{\sigma}_X, \boldsymbol{\xi}_X, \boldsymbol{\kappa}_X}(\mathbf{x})\| / \sqrt{1 - \hat{f}(\mathbf{x})^2} \right),$$

where $p_{\boldsymbol{\sigma}_Y, \boldsymbol{\xi}_Y, \boldsymbol{\kappa}_Y}^{-1}$ is the inverse of the Pareto transformation (4.1).

PREDICTION STEP

INPUT: New observation \mathbf{X}_{new} (with unobserved associated target Y_{new}) such that $\mathbf{X}_{new} \not\leq \mathbf{t}_X$.

OUTPUT of the prediction step: Predicted target $\hat{Y} = \hat{g}(\mathbf{X}_{new})$.

4.3 Distribution regression based on parametric multivariate generalized Pareto modelling

As an alternative to the point prediction strategy described in the previous paragraph, we consider a distribution regression strategy relying on parametric modelling of extreme observations transformed to exponential scale. The procedure is outlined in Algorithm 3, which we refer to as MGPREDD (Multivariate Generalized Pareto modelling for Prediction). Given the parameters $\boldsymbol{\sigma}, \boldsymbol{\xi}, \boldsymbol{\kappa} = (\boldsymbol{\sigma}_X, \boldsymbol{\sigma}_Y), (\boldsymbol{\xi}_X, \boldsymbol{\xi}_Y), (\boldsymbol{\kappa}_X, \boldsymbol{\kappa}_Y)$ estimated by Algorithm 1, we denote by $e_{\boldsymbol{\sigma}, \boldsymbol{\xi}, \boldsymbol{\kappa}}$ the specific instance of the componentwise standardization function e defined in (3.7), with marginal distributions chosen as the fitted EGP distributions, namely

$$e_{\boldsymbol{\sigma}, \boldsymbol{\xi}, \boldsymbol{\kappa}}(\mathbf{z}) = \left(-\log(1 - F_{\boldsymbol{\sigma}_X, \boldsymbol{\xi}_X, \boldsymbol{\kappa}_X}((z_1, \dots, z_d))), -\log(1 - F_{\boldsymbol{\sigma}_Y, \boldsymbol{\xi}_Y, \boldsymbol{\kappa}_Y}(z_{d+1})) \right). \quad (4.3)$$

Similarly to the Pareto marginal transformation p , we denote $e_{\boldsymbol{\sigma}_X, \boldsymbol{\xi}_X, \boldsymbol{\kappa}_X}$ and $e_{\boldsymbol{\sigma}_Y, \boldsymbol{\xi}_Y, \boldsymbol{\kappa}_Y}$ simply as e for conciseness when clear from the context. Note that the former always applies to a quantity homogeneous to \mathbf{X} , while the latter

applies to a quantity homogeneous to Y . In view of (3.8), it is asymptotically justified to fit a standard MGP model (*i.e.* a model for \mathbf{Z}'_{∞} in the latter equation) to exceedances of extreme data in \mathcal{D}_{ext} transformed to exponential margins, above the transformed threshold $e_{\sigma, \xi, \kappa}(\mathbf{t})$, where we recall that \mathbf{t} is the multivariate threshold selected *via* Algorithm 1. Thus, inference in MGPREP use as a training transformed dataset

$$\mathcal{D}_{expo} = \{e_{\sigma, \xi, \kappa}(\mathbf{Z}_i) - e_{\sigma, \xi, \kappa}(\mathbf{t})\}_{1 \leq i \leq k}$$

used for fitting standard MGP models. Here following the approach developed in Kiriliouk et al. (2019), we consider a panel $\mathcal{H} = \{\mathcal{H}_1, \dots, \mathcal{H}_M\}$ of parametric models accounting for density models for \mathbf{T} in (3.9). Using the same families, an alternative method to construct standard MGP densities is explored (related to vector \mathbf{U} in Kiriliouk et al. (2019), see Appendix C.1 for details).

During the training step of MGPREP, following Kiriliouk et al. (2019), a censored likelihood approach is employed to fit each parametric model \mathcal{H}_m . This means that only observations \mathbf{Z}_i such that all $d + 1$ components $Z_{i,j}$ are larger than t_j are used to fit the models. This censored likelihood inference step results in a family of M fitted joint densities $\{\hat{h}_m\}_{1 \leq m \leq M}$, modelling standardized and shifted excesses above threshold, namely, modelling the random vector $e_{\sigma, \xi, \kappa}(\mathbf{Z}) - e_{\sigma, \xi, \kappa}(\mathbf{t})$, as a standard MGP random vector $\mathbf{Z}'_{\infty} \in \mathbb{R}^{d+1}$. Model selection is then performed *via* a simple information criterion, *e.g.* the AIC, and the final output of the training step is a density function \hat{h} .

During the prediction step, MGPREP provides an estimate of the conditional distribution of Y_{new} given \mathbf{X}_{new} , under the form of a Monte-Carlo sample $\mathcal{D}_Y^{MC} = \{\hat{Y}_\ell\}_{1 \leq \ell \leq L}$. As an immediate by-product, a point prediction \hat{Y} can be derived as the conditional expectation of Y_{new} given \mathbf{X}_{new} , which is estimated by simply averaging the Monte-Carlo sample. The sample \mathcal{D}_Y^{MC} is obtained from the following steps: First the new observation is transformed to exponential margins and shifted by the same operations as the ones performed during the training step. The resulting variable is given by $e(\mathbf{X}_{new}) - e(\mathbf{t}_X)$. Then the conditional density of $e(Y) - e(t_Y)$ conditional on $e(\mathbf{X}_{new}) - e(\mathbf{t}_X)$ is given by $\hat{h}(\cdot | e(\mathbf{X}_{new}) - e(\mathbf{t}_X)) = \hat{h}(e(\mathbf{X}_{new}) - e(\mathbf{t}_X), \cdot) / C$ where $C = \int_{\mathbb{R}} \hat{h}(e(\mathbf{X}_{new}) - e(\mathbf{t}_X), s) ds$ is a normalizing constant. A practical Monte Carlo method for sampling from a density known only up to a normalizing constant is the Accept-Reject algorithm (see *e.g.*, Robert et al. (2010, Chapter 2)). Notably, the constant C does not need to be explicitly computed to apply this method. Finally, the latter Monte-Carlo sample is transformed back to the original scale by inverting the transformation steps using $e_{\sigma_Y, \xi_Y, \kappa_Y}^{-1}$.

In this work, MGPREP serves as a natural example of parametric modelling for conditional inference of extremes, offering a point of comparison with the Machine Learning-based ROXANE algorithm described in the previous section. During the training step, it may be viewed as a simplified version of the approach developed in Kiriliouk et al. (2019) which simultaneously fits the parameters of the marginal distribution, together with the parameters of the MGP model. The advantage of the latter joint fitting strategy is that uncertainty stemming from marginal estimation may be taken into account. However preliminary experiments (not shown) on the dataset considered here demonstrated poorer performance compared to the two-step strategy implemented in this study. This was observed in two aspects. First, as expected, the computational cost of the joint fitting procedure was significantly higher, requiring optimization steps over 7 to 11 parameters simultaneously. Second, the model fit was less satisfactory. We attribute this lack of fit to potential failures of the optimization routine which may depend on its starting point, given that the joint likelihood function is not convex. For this reason, we restrict our presentation to the two-stage model fitting process: marginal fitting using Algorithm 1, followed by multivariate model fitting on exponential marginal scale during the training phase of MGPREP. During the prediction step, MGPREP bears similarities to the methodology developed by Legrand et al. (2023) in a different context, namely for joint and conditional simulation of extreme waves. The key distinctions in our implementation for the specific use case considered here are: (i) The threshold selection is driven by marginal EGP distribution fitting; (ii) Our procedure is capable of handling three or more stations, whereas their approach heavily depends on the assumption of working with only two measurement stations; (iii) The downstream task is to reconstruct missing data based on their conditional distribution given observed neighbouring gauges, not to generate synthetic data, although Monte-Carlo sampling is used as a technical tool in our approach. Also our final averaging step for missing data imputation is not required in Legrand et al. (2023).

5 Results

The two algorithmic procedures described in Section 4 are applied to the skew surge exceedance datasets. The training dataset consists of 9,213 observations spanning the period from 10 August 1966 to 31 December 1999, while the test dataset includes 6,024 observations covering 1 January 2000 to 31 December 2023. Sections 5.1

Algorithm 3 MGPREd algorithm.

TRAINING STEP**INPUT:**

- The output of Algorithm 1 applied independently to each marginal dataset $\{Z_{i,j}\}_{1 \leq i \leq n}$ for $1 \leq j \leq d+1$: EGP parameters $\boldsymbol{\sigma}, \boldsymbol{\xi}, \boldsymbol{\kappa} = (\sigma_X, \sigma_Y), (\xi_X, \xi_Y), (\kappa_X, \kappa_Y) \in \mathbb{R}^{d+1}$; A multivariate threshold $\mathbf{t} = (t_X, t_Y) \in \mathbb{R}^{d+1}$; Extreme training dataset made of observations such that $\mathbf{X} \not\leq \mathbf{t}_X$, $\mathcal{D}_{ext} = \{\mathbf{Z}_1, \dots, \mathbf{Z}_k\}$ where $\mathbf{Z}_i = (\mathbf{X}_i, Y_i) \in \mathbb{R}^{d+1}$ represents a covariate-target pair.
- A panel of M candidate parametric models for MGP data with exponential margins as in (3.9), namely a panel $\mathcal{H} = \{\mathcal{H}_1, \dots, \mathcal{H}_M\}$ of M parametric families of density functions.

Extreme data transformation to exponential margins and shifting: Apply the exponential componentwise transformation $e_{\boldsymbol{\sigma}, \boldsymbol{\xi}, \boldsymbol{\kappa}}$ defined in (4.3) to extreme observations in \mathcal{D}_{ext}

$$e_{\boldsymbol{\sigma}, \boldsymbol{\xi}, \boldsymbol{\kappa}}(\mathbf{Z}_i), \quad \text{for } 1 \leq i \leq k \text{ (equivalently for } \mathbf{Z}_i \in \mathcal{D}_{ext}).$$

Transform the threshold \mathbf{t} as $e_{\boldsymbol{\sigma}, \boldsymbol{\xi}, \boldsymbol{\kappa}}(\mathbf{t})$.

Model fitting and model selection: Fit (through a maximum-censored likelihood method) each parametric model \mathcal{H}_m , for all $1 \leq m \leq M$, to the shifted exponential margin, extreme data

$$\mathcal{D}_{expo} = \{e_{\boldsymbol{\sigma}, \boldsymbol{\xi}, \boldsymbol{\kappa}}(\mathbf{Z}_i) - e_{\boldsymbol{\sigma}, \boldsymbol{\xi}, \boldsymbol{\kappa}}(\mathbf{t})\}_{1 \leq i \leq k}.$$

Among the fitted density functions $\hat{h}_1, \dots, \hat{h}_M$, select the density $\hat{h} \in \{\hat{h}_1, \dots, \hat{h}_M\}$ with the smallest AIC.

OUTPUT of the training step: Fitted joint density function \hat{h} in \mathcal{H} defined on \mathbb{R}^{d+1} .

PREDICTION STEP

INPUT: A new observation $\mathbf{X}_{new} \in \mathbb{R}^d$ such that $\mathbf{X}_{new} \not\leq \mathbf{t}_X$, and a Monte-Carlo sample size L .

Conditional Monte-Carlo sampling: Generate a sample of size L , $\{Y_1^e, \dots, Y_L^e\}$ from the conditional density of $\hat{h}(\cdot | e_{\boldsymbol{\sigma}_X, \boldsymbol{\xi}_X, \boldsymbol{\kappa}_X}(\mathbf{X}_{new}) - e_{\boldsymbol{\sigma}_X, \boldsymbol{\xi}_X, \boldsymbol{\kappa}_X}(\mathbf{t}_X))$ defined above.

Back-transformation: Define $\hat{Y}_\ell = e_{\boldsymbol{\sigma}_Y, \boldsymbol{\xi}_Y, \boldsymbol{\kappa}_Y}^{-1}(Y_\ell^e + e_{\boldsymbol{\sigma}_Y, \boldsymbol{\xi}_Y, \boldsymbol{\kappa}_Y}(t_Y))$, $1 \leq \ell \leq L$; and form the Monte-Carlo sample on the original scale, $\mathcal{D}_Y^{MC} = \{\hat{Y}_\ell\}_{1 \leq \ell \leq L}$.

OUTPUT of the prediction step:

- Conditional distribution of Y_{new} given the observed covariate \mathbf{X}_{new} represented by the Monte-Carlo sample \mathcal{D}_Y^{MC} (amenable to prediction intervals such as the interquartile range)
- Predicted value \hat{Y} for Y_{new} by Monte-Carlo average $\hat{Y} = L^{-1} \sum_{\ell=1}^L \hat{Y}_\ell$.

and 5.2 present the results for the fitted marginal models and the trained prediction models, respectively. Additional analyses involving similar studies on sea levels, as well as data from the Concarneau and Le Crouesty stations as output locations, are deferred to Section D of the Appendix. Section 5.3 provides a discussion and comparison of the various models. Finally, in Section 5.4, the models are applied to reconstruct the extreme skew surge time series at Port Tudy prior to the deployment of its tide gauge.

5.1 Marginal fitting and threshold selection

The initial step common to both procedures involves modelling the marginal distributions using the EGP distribution and computing the thresholds as described in Algorithm 1. The marginal fit of the training data is performed with the R package GAMLSS (R. A. Rigby and D. M. Stasinopoulos, 2005), employing the function from Carrer and Gaetan (2022). We denote by $\mathbf{t} := (t_B, t_N, t_Y)^T$ the multivariate threshold and by $\boldsymbol{\sigma} := (\sigma_B, \sigma_N, \sigma_Y)^T$, $\boldsymbol{\xi} := (\xi_B, \xi_N, \xi_Y)^T$ and $\boldsymbol{\kappa} := (\kappa_B, \kappa_N, \kappa_Y)^T$ the EGP parameters resulting from the application of Algorithm 1. The estimated parameters are presented in Table 1. Histogram plots with the corresponding fitted densities are shown in Figure 3. After thresholding, the final training sets consist of 3,269 skew surge exceedances, while final test sets consists of 2,041 skew surge exceedances.

We recall that Figure 2 presents pairwise plot of skew surge exceedances of stations. These plots illustrate

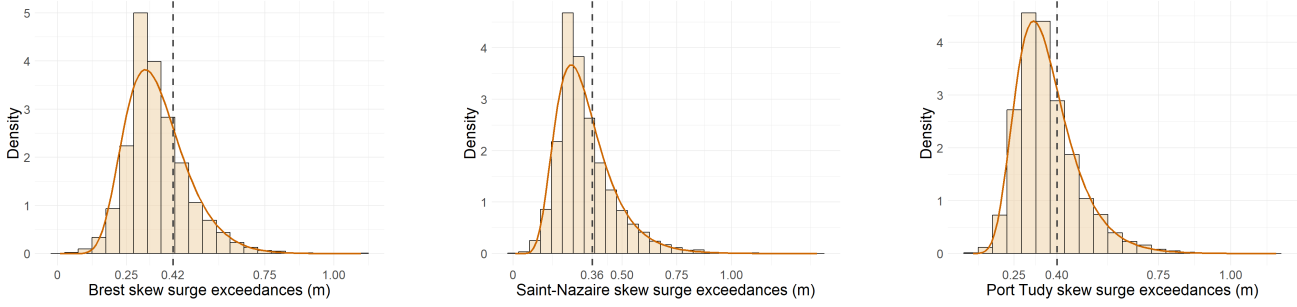


Figure 3: Histograms of skew surge exceedances at the three stations Brest (left), Saint-Nazaire (middle) and Port Tudy (right), from 01/12/2000 to 31/12/2023. The orange curves represent the fitted EGP densities, with parameters specified in Table 1. The dotted vertical grey lines represent the smallest point above which each fitted density is convex, which represent the chosen marginal thresholds via Algorithm 1 (see Section 5.1).

the strong correlation between stations, although this linear dependence is notably weaker for the most extreme observations.

Table 1: Point estimates of the parameters of the fitted EGP distribution for skew surge exceedances at the three stations. The chosen thresholds, determined using via Algorithm 1, are shown in the t rows. The data used for inference are from the training set ranging from 01/12/2000 to 31/12/2023.

PARAMETERS/STATIONS	BREST	SAINT-NAZAIRE	PORT TUDY
σ	0.13	0.10	0.09
ξ	-0.092	0.004	-0.010
κ	15.12	13.05	38.68
t	0.42	0.36	0.40

5.2 Modeling multivariate dependencies

The multivariate procedures presented in the sections 4.2 and 4.3 are now applied to the extreme skew surge exceedance observations. Recall that the selected thresholds and EGP parameters for each margin, computed on the training set are summarized in Table 1.

5.2.1 Regression method: ROXANE

Following the steps of Algorithm 2, we transformed the data to the Pareto scale so that

$$p_{\sigma, \xi, \kappa}(\mathbf{Z}_i) = (p_{\sigma_{X_B}, \xi_{X_B}, \kappa_{X_B}}(X_{B,i}), p_{\sigma_{X_N}, \xi_{X_N}, \kappa_{X_N}}(X_{N,i}), p_{\sigma_Y, \xi_Y, \kappa_Y}(Y_i))^T,$$

which is shortly denoted by $p_{\sigma, \xi, \kappa}(\mathbf{Z}_i) = (p(X_{B,i}), p(X_{N,i}), p(Y_i))^T$ when clear from the context. We then consider the angular parts of the input and the output variables w.r.t. the L^2 -norm which are given by

$$\Theta_{X,i} := (\Theta_{B,i}, \Theta_{N,i})^T := \frac{(p(X_{B,i}), p(X_{N,i}))^T}{\sqrt{p(X_{B,i})^2 + p(X_{N,i})^2}},$$

$$\Theta_{Y,i} := \frac{p(Y_i)}{\sqrt{p(X_{B,i})^2 + p(X_{N,i})^2 + p(Y_i)^2}}.$$

We employ two regression algorithms to learn a prediction function mapping the angular input observations $\Theta_{X,i}$ to the angular output observations $\Theta_{Y,i}$: Ordinary Least Squares (OLS), implemented in the STATS package, and Random Forest (RF), implemented in the RANDOMFOREST package. Based on the scatterplot shown in Figure 2, a

linear model, as assumed in the OLS approach, appears to be the most suitable choice. However, for completeness and to highlight the flexibility of the ROXANE procedure in higher dimensions, we also present results obtained using the RF algorithm, which is designed for high-dimensional data. The depth of the trees in the RF algorithm is selected using a cross-validation procedure on the training set.

Following the equivalence (4.2), the predicted angular values $\hat{\Theta}_{Y,i}$ on the test set are then backtransformed to the Pareto scale via

$$\widehat{p(Y_i)} = \frac{\hat{\Theta}_{Y,i} \sqrt{p(X_{B,i})^2 + p(X_{N,i})^2}}{\sqrt{1 - \hat{\Theta}_{Y,i}^2}},$$

and then backtransformed to the original scale via the inverse function $p_{\sigma_Y, \xi_Y, \kappa_Y}^{-1}$. As visual goodness-of-fit assessments, the left and middle columns of Figure 4 depict QQ-plots of the observed skew surge exceedances against the estimated values with the OLS algorithm and RF algorithm on the test set. In addition, Figure 5 shows the predicted curves, along with 0.95-bootstrap confidence intervals computed from the generated sample on the years 1989, 1978 and 1977, years characterized by significant skew surges at the Port Tudy tide gauge.

5.2.2 Plug-in method: MGPREP

The routine of MGPREP is described in two stages: the modelling step, followed by the prediction step. The modelling step used an adaptation of the procedure in Kiriliouk et al. (2019) to obtain a joint density model for our data, while the prediction step employs a Monte Carlo procedure to obtain an estimate using the density learnt in the modelling step.

Modelling of the data. As suggested in Algorithm 3, the extreme observations are transformed to an exponential scale and then relocated by subtracting the corresponding threshold in exponential scale $e_{\sigma, \xi, \kappa}(\mathbf{t})$ such that

$$e_{\sigma, \xi, \kappa}(\mathbf{Z}_i) - e_{\sigma, \xi, \kappa}(\mathbf{t}) = (e(X_{B,i}) - e(t_B), e(X_{N,i}) - e(t_N), e(Y_i) - e(t_Y))^T$$

where indices are again omitted for clarity.

The density models used to construct standard MGP densities are the same as those in Kiriliouk et al. (2019), stemming from multivariate distributions with independent components, where the marginal distributions are either all reverse exponential or all Gumbel distributions. To facilitate sampling in the prediction step from these distributions and avoid complex approximations, we limit our analysis to densities that do not involve unknown integral quantities. Section C.1 of the Appendix provides details on the construction of MGP densities, while Section C.2 presents the closed-form expressions for the considered densities. Again, as in Kiriliouk et al. (2019), we select a density using a censored likelihood criterion, maximizing the classic product likelihood function using only uncensored observations, where an observation is considered censored if any of its components is negative. This choice focuses the fit on the most extreme observations, which are of prime interest. After application of this procedure, the selected density model for $e_{\sigma, \xi, \kappa}(\mathbf{Z}) - e_{\sigma, \xi, \kappa}(\mathbf{t})$ is associated with independent Gumbel components with a unique dependence parameter $\alpha = 1.86$ and varying locations parameters $\beta = (\beta_B, \beta_N, \beta_Y)^T = (-0.27, 0.04, 0)^T \in \mathbb{R}^3$ given by

$$h(\mathbf{x}) = \mathbb{1}\{\max(\mathbf{x}) > 0\} \alpha^2 \Gamma(3) \exp\left(-\max(\mathbf{x}) \frac{\prod_{j \in \{B, N, Y\}} \exp(\alpha(x_j - \beta_j))}{\sum_{j \in \{B, N, Y\}} \exp(\alpha(x_j - \beta_j))}\right),$$

for $\mathbf{x} = (x_B, x_N, x_Y)^T$ and where Γ is the classic Γ -function. Note that $\beta_Y = 0$ for identifiability purpose.

Predictions on the test set. To obtain predictions for the extreme Port Tudy values in the test set, we sample 100 values through rejection sampling for each conditional densities

$$h(\cdot \mid e(X_{B,i}) - e(t_B), e(X_{N,i}) - e(t_N)) = \frac{h((e(X_{B,i}) - e(t_B), e(X_{N,i}) - e(t_N), \cdot)^T)}{\int_{\mathbb{R}} h((e(X_{B,i}) - e(t_B), e(X_{N,i}) - e(t_N), s)^T) ds}.$$

As outlined in Section 4.3, computing the normalizing constant in the denominator is not required for applying the rejection sampling method. However, approximating this constant can significantly enhance computational efficiency by ensuring the resulting function closely approximates a valid density. In our implementation, we use the numerical routine INTEGRATE to compute this approximation. For the dominant densities required in the rejection sampling method, we employ Student-t distributions, which have heavier tails than the densities of h_T . These distributions are centred at the mean of $e(X_{B,i}) - e(t_B)$ and $e(X_{N,i}) - e(t_N)$, that is, at $(e(X_{B,i}) - e(t_B) + e(X_{N,i}) - e(t_N))/2$.

The generated values in exponential scale are then backtransformed to original scale via the inverse function $e_{\sigma_Y, \xi_Y, \kappa_Y}^{-1}(\cdot + e(t_Y))$. Point estimates are obtained as Monte Carlo averages over the 100 generated values. The right column of Figure 4 presents a QQ-plot comparing the observed values with the predicted skew surge exceedances, while Figure 5 illustrates the predicted curves along with 0.95-bootstrap prediction confidence intervals computed from the generated sample for the years 1989, 1978, and 1977. The 0.95-coverage probability for these intervals is 0.89 for skew surges, where the 0.95-coverage probability is defined as the proportion of test observations that fall within the computed 0.95-prediction confidence intervals.

5.3 Discussion and comparison of the methods

In this section, we discuss the results of the marginal modelling and of both multivariate procedures. First, the EGP distribution successfully models the margins, particularly in the right tail of the distribution for data exceeding the selected thresholds, as illustrated in Figure 3. The threshold is selected as the lowest value above which the EGP density becomes strictly convex, based on the property that the GP distribution is strictly convex for $\xi > -1/2$ and that the EGP distribution closely behaves as the GP distribution in the right tail. It is therefore reasonable to consider the GP distribution as a suitable model for the data above this threshold. To validate this approach, Figure 6 presents a comparison between the EGP-fitted and GP-fitted densities above the thresholds. The two densities are remarkably similar; in the Port Tudy case, they are nearly indistinguishable, assessing the reliability of our method for selecting thresholds above which data could be considered in the extreme regime, *i.e.*, above which the GP distribution is an appropriate model.

Regarding the joint models, both procedures exhibit reasonably good performance, as evidenced by Figures 4 and 5. According to the QQ-plots, the generated distributions closely mimic the behaviour of the observed distributions in the most extreme regions. For the left tail of the extreme observations, the QQ-plots in Figure 4 indicate poor model performance. This issue is further illustrated in Figure 5, where the largest misestimations occur for the smallest values. Several factors contribute to these shortcomings. First, in MGPRED, a censored likelihood is used to focus on accurately predicting the most extreme observations, at the expense of smaller ones. Second, common to both procedures, the estimation of the κ parameter lacks robustness and is prone to significant overestimation. Although this parameter does not affect the most extreme observations, it can have a considerable impact on the smallest ones. Since the back-transformation $p_{\sigma_Y, \xi_Y, \kappa_Y}^{-1}$ behaves as $x^{1/\kappa}$ near zero, a small estimation error in Pareto scale could lead to an enormous estimation error in original scale. For instance, with $\kappa = 38.68$ (corresponding to κ_Y in Table 1), an error of just 0.01 in the Pareto scale results in a discrepancy of 0.89 meters in the original scale. Finally, another limitation common to both procedures is that an extreme observation may be extreme at Brest or Saint-Nazaire but not at the other two stations. Consequently, the models struggle to distinguish these cases from "typical" extreme events, where values at Port Tudy and another station are both large. This limitation could be addressed by incorporating wind-related data into the models, as wind strongly influences skew surges (Pugh and Woodworth, 2014), and wind direction plays a crucial role in storm propagation and the formation of large skew surges. Given these issues with the lower tail of the extreme distributions, the performance of both models should be evaluated primarily for the largest observations, which aligns with the goal of EVT.

Figure 5 also shows that our models are less precise for older years. One possible reason is the failure of our models to account for the time trend due to, *e.g.*, global warming (Seneviratne et al., 2021). Although we assume in our study that this trend is present for all three stations and can be ignored, if the trend behaviour differs across stations, it must be considered.

To emphasize the respective strengths of both procedures, a comparison is essential. We assess the performance of our models using the Root Mean Squared Error (RMSE) (and a Squared Standard Error (SSE)²) and Mean Absolute Error (MAE) (and a Absolute Standard Error (ASE)³) as measures of predictive performance. Table 2 contains the errors computed on the entire test set and for the most extreme part of the test set, which includes Y_i 's exceeding their empirical median computed on the extreme test set. Overall, the MGPRED procedure performs better: despite using a censored likelihood criterion, it models the smallest values more accurately than the ROXANE procedure. However, the ROXANE procedure, with its OLS predictive algorithm, performs better in the most extreme regions. This tendency is generally observed in sea level studies and when Concarneau and Le Crouesty are used as output stations (see Tables 4, 5, and 6 in the Appendix). Figure 7 presents QQ-plots comparing predicted values from different models. All three routines produce values of the same order, with larger values estimated

$${}^2\text{SSE} = \frac{1}{\sqrt{n}} \left(\frac{1}{n} \sum_{i=1}^n (Y_i - \hat{Y}_i)^2 - \left(\frac{1}{n} \sum_{j=1}^n (Y_j - \hat{Y}_j)^2 \right) \right)^{1/4}.$$

$${}^3\text{ASE} = \frac{1}{\sqrt{n}} \left(\frac{1}{n} \sum_{i=1}^n (|Y_i - \hat{Y}_i| - \left(\frac{1}{n} \sum_{j=1}^n |Y_j - \hat{Y}_j| \right)^2) \right)^{1/2}.$$

by the ROXANE algorithm in the most extreme regions, which appear to better match the true ones, as shown in Figure 4. All predicted values from the ROXANE algorithm fall within the 0.95-prediction confidence interval derived from MGPRED.

Table 2: $\text{RMSE} \cdot 10^2 (\text{SSE} \cdot 10^2)$ and $\text{MAE} \cdot 10^2 (\text{ASE} \cdot 10^2)$ of predicted skew surge exceedances at Port Tudy station from the ROXANE procedure with RF regression (ROX RF), ROXANE procedure with OLS regression (ROX OLS) and MGPRED. Errors are measured on the test set covering the period from 10/08/1966 to 31/12/1999. Errors are computed for the entire test set (columns: RMSE and MSE) and for the subset of the test set comprising the most extreme observations w.r.t. the Port Tudy observations, *i.e.*, observations such that $Y_i \geq q_Y^{\text{ext}, 0.5}$ (columns: RMSE_{EXT} and MAE_{EXT}).

TRAINING MODELS/ERRORS	RMSE	MAE	RMSE_{EXT}	MAE_{EXT}
ROX RF	8.3(0.3)	5.8(0.1)	7.5(0.3)	5.4(0.2)
ROX OLS	8.2(0.3)	5.7(0.1)	7.4(0.3)	5.3(0.2)
MGPRED	7.6(0.2)	5.5(0.1)	7.8(0.4)	5.7(0.2)

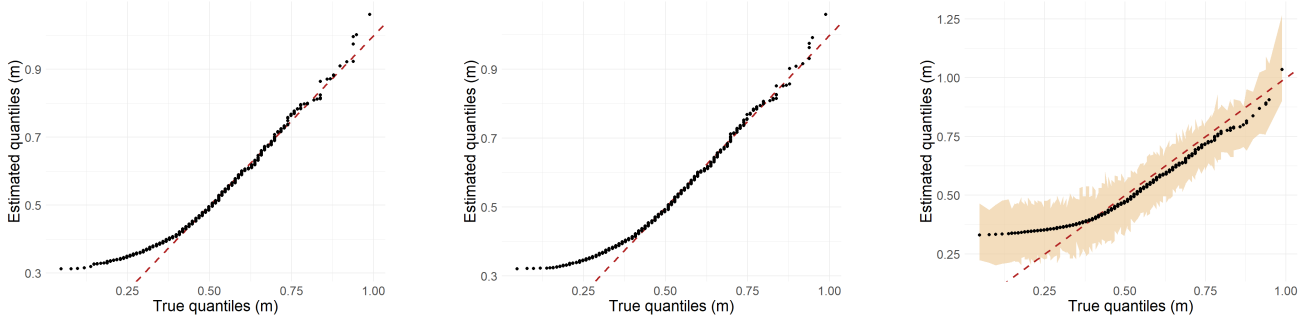


Figure 4: QQ-plots comparing observed skew surge exceedances of the Port Tudy test set (x-axis), ranging from 10/08/1966 to 31/12/1999, to predicted data (y-axis) from the algorithms of Sections 4.2 and 4.3. The plots show results from the ROXANE procedure with RF regression (left), ROXANE procedure with OLS regression (middle), and MGPRED (right) with bootstrap 0.95 confidence bands (lightorange). The dotted red line represents the identity line $x = y$.

5.4 Extreme skew surges time series reconstruction

This section presents the results of reconstructing extreme skew surge time series at the Port Tudy tide gauge prior to its deployment on August 10, 1966. The reconstruction uses historical data from the Brest and Saint-Nazaire tide gauges, the latter of which has recorded measurements since January 18, 1863. New predictive models were trained using observations collected during the overlapping operational period of the three tide gauges, spanning from August 10, 1966, to December 31, 2023. This period corresponds to what was previously designated as the training and test sets into a unified training dataset. The training procedures described in the sections 5.1 and 5.2, as well as preceding sections, are strictly applied.

Figure 8 illustrates the extreme skew surge time series at Brest and Saint-Nazaire, distinguishing between the training and reconstruction periods. Although the reconstruction period is longer than the training period, it contains fewer data points, likely due to gaps in historical records at Brest and Saint-Nazaire before 1966. Specifically, the average number of annual measurements prior to August 10, 1966, is 319, compared to 539 per year thereafter. Additionally, previous studies (e.g., Bardet et al. (2011)) indicate a positive trend in skew surges along the French Atlantic coast, suggesting that thresholds established from post-1966 data may correspond to more extreme conditions when applied to pre-1966 data. However, no discernible trend is observed for the most extreme skew surges, as evidenced by the Saint-Nazaire time series in Figure 8.

Figure 9 presents the predicted time series generated by the ROXANE routine using both the OLS and RF algorithms, and by MGPRED. All methods exhibit substantial limitations in predicting smaller extreme values, as

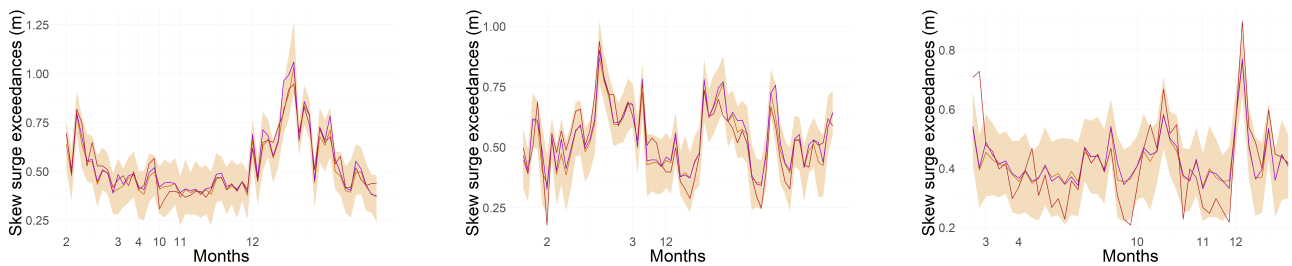


Figure 5: Predicted skew surge exceedances at Port Tudy station for the years 1989 (left), 1978 (middle), 1977 (right). Red curves represent the true values; purple curves represent the predicted values by the ROXANE procedure with OLS algorithm; orange curves represent the predicted values by MGPRED with bootstrap 0.95 confidence bands (lightorange).

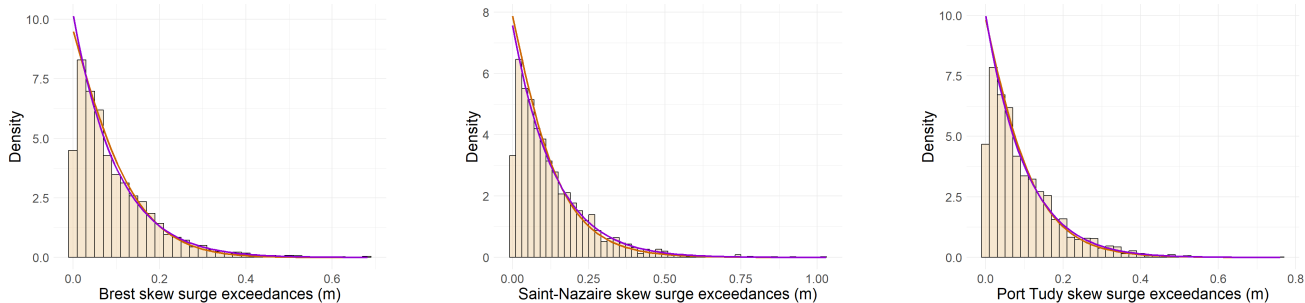


Figure 6: Histograms of skew surge exceedances above the threshold specified in Table 1 at the three stations Brest (left), Saint-Nazaire (middle) and Port Tudy (right), from 01/12/2000 to 31/12/2023. The orange curves represent the fitted EGP densities above the thresholds, with parameters specified in Table 1. The purple curves represent the fitted GP densities.

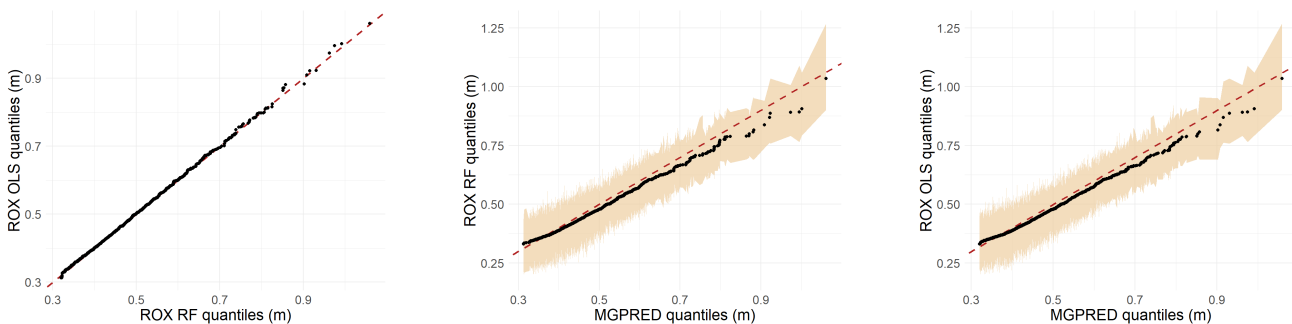


Figure 7: QQ-plots comparing predicted skew surge exceedances of the Port Tudy test set, ranging from 10/08/1966 to 31/12/1999, from the algorithms of Sections 4.2 and 4.3: ROX RF *vs* ROX RF (left), MGPRED *vs* ROX RF (middle), and MGPRED *vs* ROX OLS (middle), with bootstrap 0.95 confidence bands (lightorange) from MGPRED. The dotted red line represents the identity line $x = y$.

discussed in Section 5.3, with only a few slightly negative skew surge predictions. However, the estimated largest skew surges align closely with observed values in the training set and with the input data from the reconstruction period, as illustrated in Figures 8 and 9. This consistency in predicting extreme values is further corroborated by Figure 10, which depicts pairwise scatter plots of predictions against observed input values, revealing patterns similar to those observed in the training set scatter plot (Figure 2).

Consistent with previous findings, the ROXANE procedure tends to predict larger extreme surges compared to MGPRED. The largest skew surges predicted by both models are associated with significant skew surges recorded at Brest and/or Saint-Nazaire. However, a notable discrepancy arises in the case of December 10, 1957: while the ROXANE algorithm predicts this event as the largest extreme skew surge, MGPRED estimates only a moderately extreme surge. This difference underscores a fundamental distinction between the two approaches. The ROXANE

procedure assigns greater weight to extreme values recorded at any individual input station, whereas MGPREP prioritizes events where the mean of both input values is large. For example, the most extreme skew surge recorded at Brest prior to August 10, 1966, occurred on December 10, 1957, while the corresponding value at Saint-Nazaire was only moderate. In such cases, the ROXANE procedure may be more appropriate, as a significant surge at a single input station could plausibly result in a large surge at the output station. As previously noted, incorporating wind-related variables may enhance both procedures, leading to more reliable predictions in this case.

A more comprehensive assessment of the reconstruction accuracy could be achieved by analysing historical meteorological records and archives at Port Tudy to identify correspondences between significant climatic events and predicted extreme surges. However, such an analysis is beyond the scope of the present study and is left for future research.

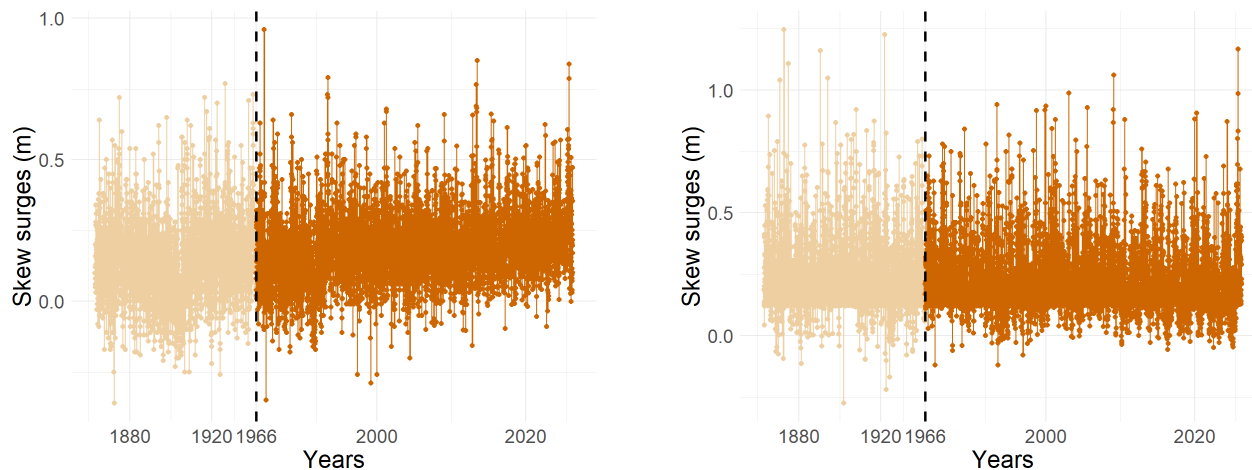


Figure 8: Extreme skew surge time series at Brest (left) and Saint-Nazaire (right). The dotted vertical black line represents the deployment date of the tide gauge at Port Tudy (10/08/1966). The dark orange points represent values after 10/08/1966, used for training the prediction models; the light orange points represent values before 10/08/1966, corresponding to the reconstruction period of the Port Tudy time series.

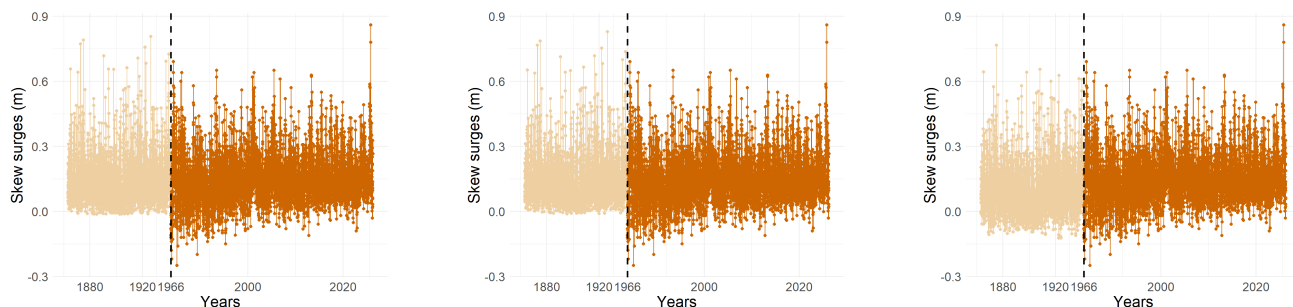


Figure 9: Extreme skew surge time series at Brest (left) and Saint-Nazaire (right). The dotted vertical black line represents the deployment date of the tide gauge at Port Tudy (10/08/1966). The dark orange points represent values after 10/08/1966, used for training the prediction models; the light orange points represent the predicted values by the ROXANE procedure with OLS (left), RF (middle) algorithms and by MGPREP (right) before 10/08/1966.

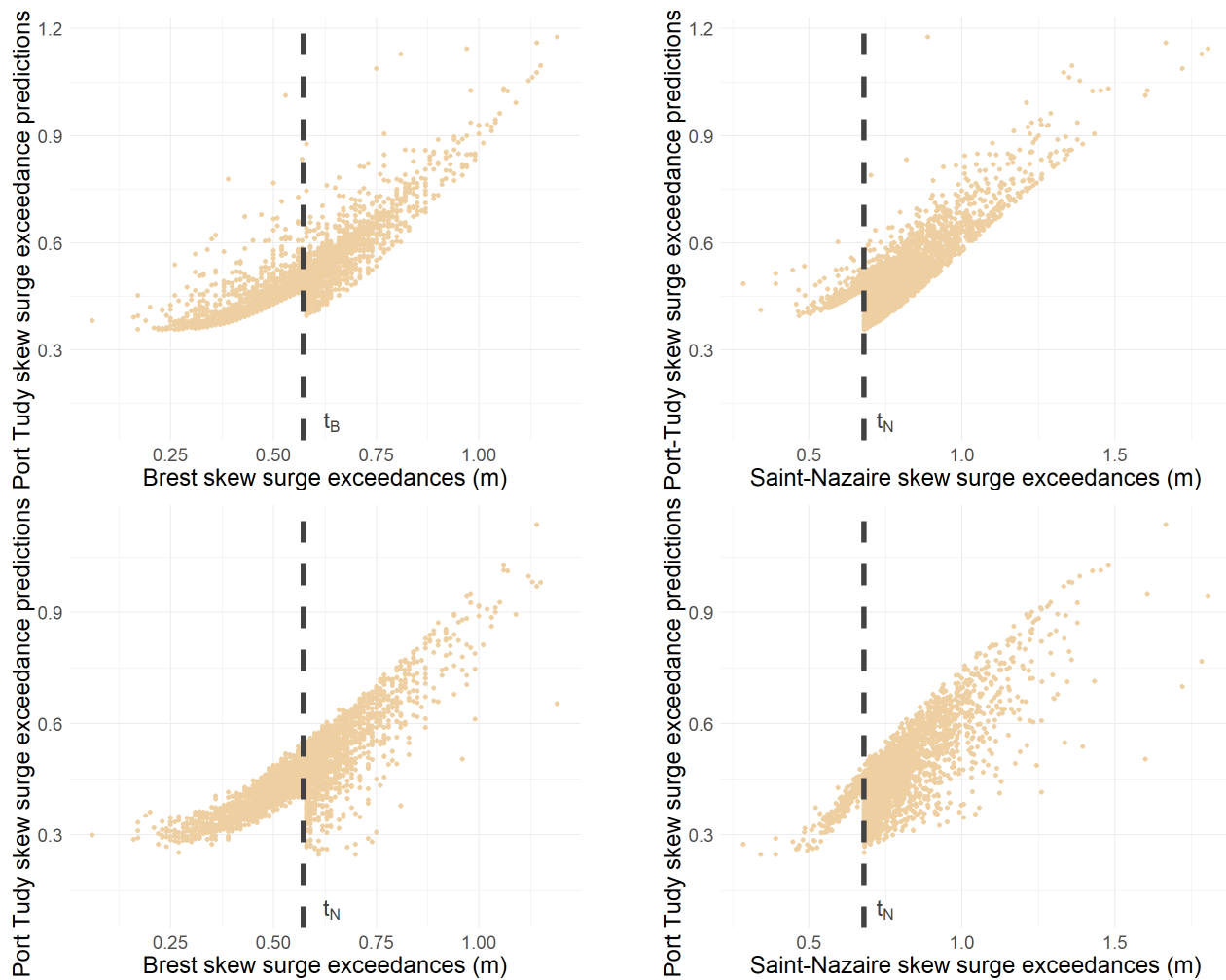


Figure 10: Predicted skew surges (y-axis), by the ROXANE procedure with OLS algorithm (top row) and the MGP procedure (bottom row), at Port Tudy before 10/08/1966 against the true values (x-axis) at Brest (left) and at Saint-Nazaire (right). The black dotted lines represent the chosen marginal threshold via Algorithm 1.

6 Conclusion and Perspectives

Accurately reconstructing extreme skew surge time series is essential for refining the computation of long-range return periods, particularly at tide gauges with limited observational data. Leveraging robust theoretical results from extreme-value theory, we explore a nonparametric and a parametric multivariate methods to address the challenge of predicting sea levels and skew surges measured at tide gauges along the French Atlantic coast. These methods are comprehensively compared and analysed, demonstrating that both yield valid and practically significant results. Each approach offers distinct advantages: one excels in providing precise point estimates, while the other delivers confidence intervals for the estimates and a robust generative model. Additionally, through the use of the EGP distribution for marginal modelling, we introduce an innovative and simple method for selecting a univariate threshold above which observations belong to an extreme regime.

The proposed methods, including the marginal modelling and both multivariate prediction techniques, are broadly applicable to other contexts involving spatial extremes. Furthermore, these approaches can be extended to incorporate additional covariates to enhance prediction accuracy. For instance, the ROXANE procedure is compatible with any regression algorithm, including high-dimensional models like Random Forest regression. Incorporating wind-related measurements at input stations could address the challenges associated with estimating smaller extreme observations. These extensions are left to further research.

Acknowledgments

We thank Dr. Gael André (SHOM) and Dr. Xavier Kerdadallan (CEREMA) for their insightful discussions on sea levels and tides, in particular for the guided visit at one of the world oldest tide gauges located in Brest, France.

Conflict of interests

None declared.

Funding

Part of Naveau's research work was supported by European H2020 XAIDA (Grant agreement ID: 101003469) and the French national programs: the ANR EXSTA, and the PEPR TRACCS programme under grant number ANR-22-EXTR-0005, contrat 291716 PEPR IRIMA (SNA), PC "IRIMONT" (France 2030 ANR-22-EXIR-0003) and the Mines Paris / INRAE chair Geolearning.

Data and code availability

The dataset, alongside with the code developed for the proposed methodology, is available at github.com/HuetNathan/extremesealevels.

References

- August A Balkema and Laurens De Haan. Residual life time at great age. *The Annals of probability*, 2(5):792–804, 1974.
- Lise Bardet, C-M Duluc, Vincent Rebour, and J L’her. Regional frequency analysis of extreme storm surges along the french coast. *Natural Hazards and Earth System Sciences*, 11(6):1627–1639, 2011.
- N. Beck, C. Genest, J. Jalbert, and M. Mailhot. Predicting extreme surges from sparse data using a copula-based hierarchical bayesian spatial model. *Environmetrics*, 31(5):e2616, 2020.
- Kai Bellinghausen, Birgit Hünicke, and Eduardo Zorita. Using random forests to predict extreme sea-levels at the baltic coast at weekly timescales. *EGUsphere*, 2024:1–52, 2024.
- Pietro Bernardara, Marc Andreewsky, and Michel Benoit. Application of regional frequency analysis to the estimation of extreme storm surges. *Journal of Geophysical Research: Oceans*, 116(C2), 2011.
- Natacha B Bernier, Mark Hemer, Nobuhito Mori, Christian M Appendini, Oyvind Breivik, Ricardo de Camargo, Mercè Casas-Prat, Trang Minh Duong, Ivan D Haigh, Tom Howard, et al. Storm surges and extreme sea levels: Review, establishment of model intercomparison and coordination of surge climate projection efforts (surgemip). *Weather and Climate Extremes*, 45:100689, 2024.
- Georgios Boumis, Hamed R Moftakhari, and Hamid Moradkhani. Coevolution of extreme sea levels and sea-level rise under global warming. *Earth’s Future*, 11(7):e2023EF003649, 2023.
- Nicolas Bruneau, Jeff Polton, Joanne Williams, and Jason Holt. Estimation of global coastal sea level extremes using neural networks. *Environmental Research Letters*, 15(7):074030, 2020.
- Francisco M Calafat and Marta Marcos. Probabilistic reanalysis of storm surge extremes in europe. *Proceedings of the National Academy of Sciences*, 117(4):1877–1883, 2020.
- Noémie Le Carrer and Carlo Gaetan. Distributional regression models for extended generalized pareto distributions. *arXiv preprint arXiv:2209.04660*, 2022.
- Céline Chadenas, Axel Creach, and Denis Mercier. The impact of storm xynthia in 2010 on coastal flood prevention policy in france. *Journal of coastal conservation*, 18:529–538, 2014.
- Maël Chiapino, Anne Sabourin, and Johan Segers. Identifying groups of variables with the potential of being large simultaneously. *Extremes*, 22:193–222, 2019.
- Alba Cid, Thomas Wahl, Don P Chambers, and Sanne Muis. Storm surge reconstruction and return water level estimation in southeast asia for the 20th century. *Journal of Geophysical Research: Oceans*, 123(1):437–451, 2018.
- Daniela Cisneros, Arnab Hazra, and Raphaël Huser. Spatial wildfire risk modeling using a tree-based multivariate generalized pareto mixture model. *Journal of Agricultural, Biological and Environmental Statistics*, 29(2):320–345, 2024.
- Stephan Cléménçon and Anne Sabourin. Weak signals and heavy tails: Machine-learning meets extreme value theory. *arXiv preprint arXiv:2504.06984*, 2025.
- Stephan Cléménçon, Nathan Huet, and Anne Sabourin. Regular variation in hilbert spaces and principal component analysis for functional extremes. *Stochastic Processes and their Applications*, 174:104375, 2024.
- Thomas P Collings, Niall D Quinn, Ivan D Haigh, Joshua Green, Izzy Probyn, Hamish Wilkinson, Sanne Muis, William V Sweet, and Paul D Bates. Global application of a regional frequency analysis to extreme sea levels. *Natural Hazards and Earth System Sciences*, 24(7):2403–2423, 2024.
- Daniel Cooley and Emeric Thibaud. Decompositions of dependence for high-dimensional extremes. *Biometrika*, 106(3):587–604, 2019.
- Eleanor D’Arcy, Jonathan Tawn, Amilie Joly, and Dafni Sifnioti. Accounting for seasonality in extreme sea level estimation. *Annals of Applied Statistics*, April 2023. ISSN 1932-6157.

- Anthony C Davison and Raphaël Huser. Statistics of extremes. *Annual Review of Statistics and its Application*, 2(1):203–235, 2015.
- Mark J Dixon and Jonathan A Tawn. *Extreme sea-levels at the UK A-class sites: site-by-site analyses*. Proudman Oceanographic Laboratory, 1994.
- Holger Drees and Anne Sabourin. Principal component analysis for multivariate extremes. *Electronic Journal of Statistics*, 15:908–943, 2021.
- Sebastian Engelke and Adrien S Hitz. Graphical Models for Extremes. *Journal of the Royal Statistical Society Series B*, 82(4):871–932, 2020.
- Elisabetta Genovese and Valentin Przylyuski. Storm surge disaster risk management: the xynthia case study in france. *Journal of Risk Research*, 16(7):825–841, 2013.
- Nicolas Goix, Anne Sabourin, and Stephan Cléménçon. Sparse representation of multivariate extremes with applications to anomaly ranking. *AISTATS*, pages 75–83, 2016.
- Nicolas Goix, Anne Sabourin, and Stephan Cléménçon. Sparse representation of multivariate extremes with applications to anomaly detection. *Journal of Multivariate Analysis*, 161:12–31, 2017.
- Ludovic Harter, Lucia Pineau-Guillou, and Bertrand Chapron. Underestimation of extremes in sea level surge reconstruction. *Scientific Reports*, 14(1):14875, 2024.
- Janet E Heffernan and Jonathan A Tawn. A conditional approach for multivariate extreme values (with discussion). *Journal of the Royal Statistical Society Series B: Statistical Methodology*, 66(3):497–546, 2004.
- JRM Hosking. Regional frequency analysis, 1997.
- Nathan Huet, Stephan Cléménçon, and Anne Sabourin. On regression in extreme regions. *arXiv preprint arXiv:2303.03084*, 2023.
- Déborah Idier, Franck Dumas, and Héloïse Muller. Tide-surge interaction in the english channel. *Natural Hazards and Earth System Sciences*, 12(12):3709–3718, 2012.
- Hamid Jalalzai, Stephan Cléménçon, and Anne Sabourin. On binary classification in extreme regions. *NIPS*, pages 3092–3100, 2018.
- Anja Janßen and Phyllis Wan. k -means clustering of extremes. *Electronic Journal of Statistics*, 14(1):1211–1233, 2020.
- Svetlana Jevrejeva, Luke P Jackson, Riccardo EM Riva, Aslak Grinsted, and John C Moore. Coastal sea level rise with warming above 2 c. *Proceedings of the National Academy of Sciences*, 113(47):13342–13347, 2016.
- Tao Ji, Guosheng Li, and Rui Liu. Historical reconstruction of storm surge activity in the southeastern coastal area of china for the past 60 years. *Earth and Space Science*, 7(8):e2019EA001056, 2020.
- M Karamouz, M Taheri, P Khalili, and X Chen. Building infrastructure resilience in coastal flood risk management. *Journal of Water Resources Planning and Management*, 145(4):04019004, 2019.
- Xavier Kergadallan. Estimation des valeurs extrêmes de niveau d’eau : Littoral métropolitain. Technical report, CEREMA, 2022. URL https://doc.cerema.fr/Default/doc/SYRACUSE/593562/estimation-des-valeurs-extremes-de-niveau-d-eau-littoral-metropolitain?_lg=fr-FR.
- Xavier Kergadallan, Pietro Bernardara, Michel Benoit, and Camille Daubord. Improving the estimation of extreme sea levels by a characterization of the dependence of skew surges on high tidal levels. *Coastal engineering proceedings*, 1:48, 2014.
- Anna Kiriliouk, Holger Rootzén, Johan Segers, and Jennifer L Wadsworth. Peaks over thresholds modeling with multivariate generalized pareto distributions. *Technometrics*, 61(1):123–135, 2019.
- Juliette Legrand, Pierre Ailliot, Philippe Naveau, and Nicolas Raillard. Joint stochastic simulation of extreme coastal and offshore significant wave heights. *The Annals of Applied Statistics*, 17(4):3363–3383, 2023.

- Allan McRobie, Tom Spencer, and Herman Gerritsen. The big flood: North sea storm surge. *Philosophical Transactions of the Royal Society A: Mathematical, Physical and Engineering Sciences*, 363(1831):1263–1270, 2005.
- Nicolas Meyer and Olivier Wintenberger. Sparse regular variation. *Advances in Applied Probability*, 53(4):1115–1148, 2021.
- Nicolas Meyer and Olivier Wintenberger. Multivariate sparse clustering for extremes. *Journal of the American Statistical Association*, 0:1–23, 2023.
- JS Nanditha, Gabriele Villarini, Hanbeen Kim, and Philippe Naveau. Strong linkage between observed daily precipitation extremes and anthropogenic emissions across the contiguous united states. *Geophysical Research Letters*, 51(20):e2024GL109553, 2024.
- P. Naveau and J. Segers. Multivariate extreme value theory. In M. de Carvalho, R. Huser, P. Naveau, and B.J. Reich, editors, *Handbook on Statistics of Extremes*, chapter 7. Chapman & Hall / CRC, 2025.
- Philippe Naveau, Raphael Huser, Pierre Ribereau, and Alexis Hannart. Modeling jointly low, moderate, and heavy rainfall intensities without a threshold selection. *Water Resources Research*, 52(4):2753–2769, 2016.
- Ryo Nezaki and Hideki Nagatsuka. New anomaly detection method based on the multivariate generalized pareto distributions. *Total Quality Science*, 8(2):89–99, 2023.
- Zhenhua Pan and Hua Liu. Impact of human projects on storm surge in the yangtze estuary. *Ocean Engineering*, 196:106792, 2020.
- Ioannis Papastathopoulos and Jonathan A Tawn. Extended generalised pareto models for tail estimation. *Journal of Statistical Planning and Inference*, 143(1):131–143, 2013.
- Lucia Pineau-Guillou, Cyril Lathuiliere, Rudy Magne, Stéphanie Louazel, David Corman, and Céline Perherin. Sea levels analysis and surge modelling during storm xynthia. *European journal of environmental and civil engineering*, 16(8):943–952, 2012.
- David Pugh and Philip Woodworth. *Sea-level science: understanding tides, surges, tsunamis and mean sea-level changes*. Cambridge University Press, 2014.
- David T Pugh and JM Vassie. Extreme sea levels from tide and surge probability. *Coastal Engineering*, pages 911–930, 1978.
- DT Pugh and JM Vassie. Applications of the joint probability method for extreme sea level computations. *Proceedings of the Institution of Civil Engineers*, 69(4):959–975, 1980.
- R. A. Rigby and D. M. Stasinopoulos. Generalized additive models for location, scale and shape,(with discussion). *Applied Statistics*, 54:507–554, 2005.
- Sidney I Resnick. *Extreme values, regular variation, and point processes*, volume 4. Springer Science & Business Media, 2008.
- Pauline Rivoire, Olivia Martius, and Philippe Naveau. A comparison of moderate and extreme era-5 daily precipitation with two observational data sets. *Earth and Space Science*, 8(4):e2020EA001633, 2021.
- Christian P Robert, George Casella, and George Casella. *Introducing Monte Carlo methods with R*, volume 18. Springer, 2010.
- Holger Rootzén and Nader Tajvidi. Multivariate generalized pareto distributions. *Bernoulli*, 12(5):917–930, 2006.
- Holger Rootzén, Johan Segers, and Jennifer L. Wadsworth. Multivariate peaks over thresholds models. *Extremes*, 21(1):115–145, 2018.
- Holger Rootzén, Johan Segers, and Jennifer L. Wadsworth. Multivariate generalized pareto distributions: Parametrizations, representations, and properties. *Journal of Multivariate Analysis*, 165:117–131, 2018. ISSN 0047-259X. doi: <https://doi.org/10.1016/j.jmva.2017.12.003>. URL <https://www.sciencedirect.com/science/article/pii/S0047259X17303147>.

- Sonia I Seneviratne, Xuebin Zhang, Muhammad Adnan, Wafae Badi, Claudine Dereczynski, A Di Luca, Subimal Ghosh, Iskhaq Iskandar, James Kossin, Sophie Lewis, et al. *Weather and climate extreme events in a changing climate*. Cambridge University Press, 2021.
- Emma S Simpson, Jennifer L Wadsworth, and Jonathan A Tawn. Determining the Dependence Structure of Multivariate Extremes. *Biometrika*, 107(3):513–532, 2020.
- Michael Tadesse, Thomas Wahl, and A Cid. Data-driven modeling of global storm surges. *Frontiers in Marine Science*, 7:512653, 2020.
- Michael Getachew Tadesse and Thomas Wahl. A database of global storm surge reconstructions. *Scientific data*, 8(1):125, 2021.
- JA Tawn, JM Vassie, and EJ Gumbel. Extreme sea levels; the joint probabilities method revisited and revised. *Proceedings of the Institution of Civil Engineers*, 87(3):429–442, 1989.
- Jonathan A Tawn. Estimating probabilities of extreme sea-levels. *Journal of the Royal Statistical Society Series C: Applied Statistics*, 41(1):77–93, 1992.
- Claudia Tebaldi, Roshanka Ranasinghe, Michalis Vousdoukas, DJ Rasmussen, Ben Vega-Westhoff, Ebru Kirezci, Robert E Kopp, Ryan Sriver, and Lorenzo Mentaschi. Extreme sea levels at different global warming levels. *Nature Climate Change*, 11(9):746–751, 2021.
- Patricia Tencaliec, A-C Favre, Philippe Naveau, Clémentine Prieur, and Gilles Nicolet. Flexible semiparametric generalized pareto modeling of the entire range of rainfall amount. *Environmetrics*, 31(2):e2582, 2020.
- Maria Antónia Amaral Turkman, Kamil Feridun Turkman, Patricia de Zea Bermudez, Soraia Pereira, Paula Pereira, and Miguel de Carvalho. Calibration of the bulk and extremes of spatial data. *REVSTAT-Statistical Journal*, 19(3):309–325, 2021.
- Edoardo Vignotto, Sebastian Engelke, and Jakob Zscheischler. Clustering bivariate dependencies of compound precipitation and wind extremes over great britain and ireland. *Weather and Climate Extremes*, 32:100318, 2021.
- Michalis I Vousdoukas, Lorenzo Mentaschi, Evangelos Voukouvalas, Martin Verlaan, Svetlana Jevrejeva, Luke P Jackson, and Luc Feyen. Global probabilistic projections of extreme sea levels show intensification of coastal flood hazard. *Nature communications*, 9(1):2360, 2018.
- Matthew P Wadey, Ivan D Haigh, Robert J Nicholls, Jennifer M Brown, Kevin Horsburgh, Ben Carroll, Shari L Gallop, Travis Mason, and Elizabeth Bradshaw. A comparison of the 31 january–1 february 1953 and 5–6 december 2013 coastal flood events around the uk. *Frontiers in Marine Science*, 2:84, 2015.
- Phyllis Wan. Characterizing extremal dependence on a hyperplane. *arXiv preprint arXiv:2411.00573*, 2024.
- Jinping Wang, John A. Church, Xuebin Zhang, and Xianyao Chen. Improved sea level reconstruction from 1900 to 2019. *Journal of Climate*, 37(24):6453 – 6474, 2024.
- Ralf Weisse, Debora Bellafiore, Melisa Menéndez, Fernando Méndez, Robert J Nicholls, Georg Umgiesser, and Patrick Willems. Changing extreme sea levels along european coasts. *Coastal engineering*, 87:4–14, 2014.
- Joanne Williams, Kevin J Horsburgh, Jane A Williams, and Robert NF Proctor. Tide and skew surge independence: New insights for flood risk. *Geophysical Research Letters*, 43(12):6410–6417, 2016.

Appendix

The appendix is organized as follows: Section A provides a detailed explanation of the preprocessing steps outlined in Section 2. Section B presents a proof of the threshold formula used in Algorithm 1. Section C compiles details and closed-form expressions for the density models employed in MGPRED. Finally, Section D presents two additional analyses, analogous to those in Section 5, using sea level and skew surge data at Concarneau and Le Croesty as the output stations, along with an additional study using sea level data at Port Tudy as the output.

A Preprocessing

The original dataset comprises triplets $(X_{B,i}^{ori}, X_{N,i}^{ori}, Y_i^{ori})_{1 \leq i \leq m}$ where $X_{B,i}^{ori}, X_{N,i}^{ori}, Y_i^{ori}$ are the raw sea levels or skew surges measured respectively at Brest, Saint-Nazaire and Port Tudy. A first pre-selection is performed such that we retain only triplets such $X_{B,i}^{ori}$ or $X_{N,i}^{ori}$ exceed their empirical median *i.e.*, triplets such that $(X_{B,i}^{ori}, X_{N,i}^{ori}, Y_i^{ori})_{i \in I}$ with

$$I = \left\{ i \in 1, \dots, m, X_{B,i}^{ori} \geq q_B^{ori,\rho} \text{ or } X_{N,i}^{ori} \geq q_N^{ori,\rho} \right\},$$

where $q_B^{ori,\rho}$ (resp. $q_N^{ori,\rho}$) is the original empirical ρ -quantile at Brest (resp. at Saint-Nazaire). This operation is depicted in Figure 11. For conciseness, we assume $I = 1, \dots, n$ in the main text. Finally, the origin is shifted: we subtract, from each component of the observations, the minimum value recorded over I , *i.e.*, the observations considered in the main paper are

$$(X_{B,i}, X_{N,i}, Y_i) := (X_{B,i}^{ori} - m_B, X_{N,i}^{ori} - m_N, Y_i^{ori} - m_Y),$$

for $i \in I$ and where $m_B = \min_{i \in I} X_{B,i}^{ori}$, $m_N = \min_{i \in I} X_{N,i}^{ori}$ and $m_Y = \min_{i \in I} Y_i^{ori}$.

B Threshold Formula

A proof of the formula for the threshold given in Algorithm 1 is presented in this section.

We need to compute the second derivative of the density function $f_{\sigma,\xi,\kappa}$ (3.2) and then compute the zeros of this second derivative. Recall that the function is given by

$$f_{\sigma,\xi,\kappa}(x) = \frac{\kappa}{\sigma} \left(1 + \frac{\xi x}{\sigma}\right)^{-1/\xi-1} \left(1 - \left(1 + \frac{\xi x}{\sigma}\right)^{-1/\xi}\right)^{\kappa-1}.$$

The first and second derivatives of $f_{\sigma,\xi,\kappa}$ are

$$\frac{df_{\sigma,\xi,\kappa}(x)}{dx} = \frac{\kappa}{\sigma^2} \left((\kappa-1) \left(1 + \frac{\xi x}{\sigma}\right)^{-2/\xi-2} \left(1 - \left(1 + \frac{\xi x}{\sigma}\right)^{-1/\xi}\right)^{\kappa-2} - (\xi+1) \left(1 + \frac{\xi x}{\sigma}\right)^{-1/\xi-2} \left(1 - \left(1 + \frac{\xi x}{\sigma}\right)^{-1/\xi}\right)^{\kappa-1} \right),$$

and

$$\begin{aligned} \frac{d^2 f_{\sigma,\xi,\kappa}(x)}{dx^2} &= \frac{\kappa}{\sigma^3} \left(1 + \frac{\xi x}{\sigma}\right)^{-1/\xi-3} \left(1 - \left(1 + \frac{\xi x}{\sigma}\right)^{-1/\xi}\right)^{\kappa-3} \left[(\kappa-1)(\kappa-2) \left(1 + \frac{\xi x}{\sigma}\right)^{-2/\xi} - \right. \\ &\quad \left. (\kappa-1)(3+3\xi) \left(1 + \frac{\xi x}{\sigma}\right)^{-1/\xi} \left(1 - \left(1 + \frac{\xi x}{\sigma}\right)^{-1/\xi}\right) + (\xi+1)(1+2\xi) \left(1 - \left(1 + \frac{\xi x}{\sigma}\right)^{-1/\xi}\right)^2 \right] \\ &= \frac{\kappa}{\sigma^3} \left(1 + \frac{\xi x}{\sigma}\right)^{-1/\xi-3} \left(1 - \left(1 + \frac{\xi x}{\sigma}\right)^{-1/\xi}\right)^{\kappa-3} A \left(\left(1 + \frac{\xi x}{\sigma}\right)^{-1/\xi} \right), \end{aligned}$$

with $A(X) = (\kappa-1)(\kappa-2)X^2 - (\kappa-1)(3+3\xi)X(1-X) + (\xi+1)(1+2\xi)(1-X)^2$. The two zeros of $\frac{d^2 f_{\sigma,\xi,\kappa}(x)}{dx^2}$ associated with the two first factors of the above equation are 0 and $-\sigma/\xi$ corresponding to the lower and upper bounds of the support of the density. Therefore, the desired point lies in the zeros of $A \left(\left(1 + \frac{\xi x}{\sigma}\right)^{-1/\xi} \right)$. Note that if X_0 is a zero of A then $(\sigma/\xi)(X_0^{-\xi} - 1)$ is a zero of $A \left(\left(1 + \frac{\xi x}{\sigma}\right)^{-1/\xi} \right)$. The canonical form of A is

$$A(X) = (\kappa^2 + 2\xi^2 + 3\kappa\xi)X^2 + (4\xi^2 + 3\kappa + 3\xi + 3\kappa\xi - 1)X + (2\xi^2 + 3\xi + 1).$$

Solving the second-degree polynomial gives the largest zero of A

$$X_0 = \frac{4\xi^2 + 3\kappa\xi + 3\kappa + 3\xi - 1 - \sqrt{(4\xi^2 + 3\kappa\xi + 3\kappa + 3\xi - 1)^2 - 4(\kappa^2 + 2\xi^2 + 3\kappa\xi)(2\xi^2 + 3\xi + 1)}}{2(\kappa^2 + 2\xi^2 + 3\kappa\xi)},$$

and the threshold formula in Algorithm 1 follows.

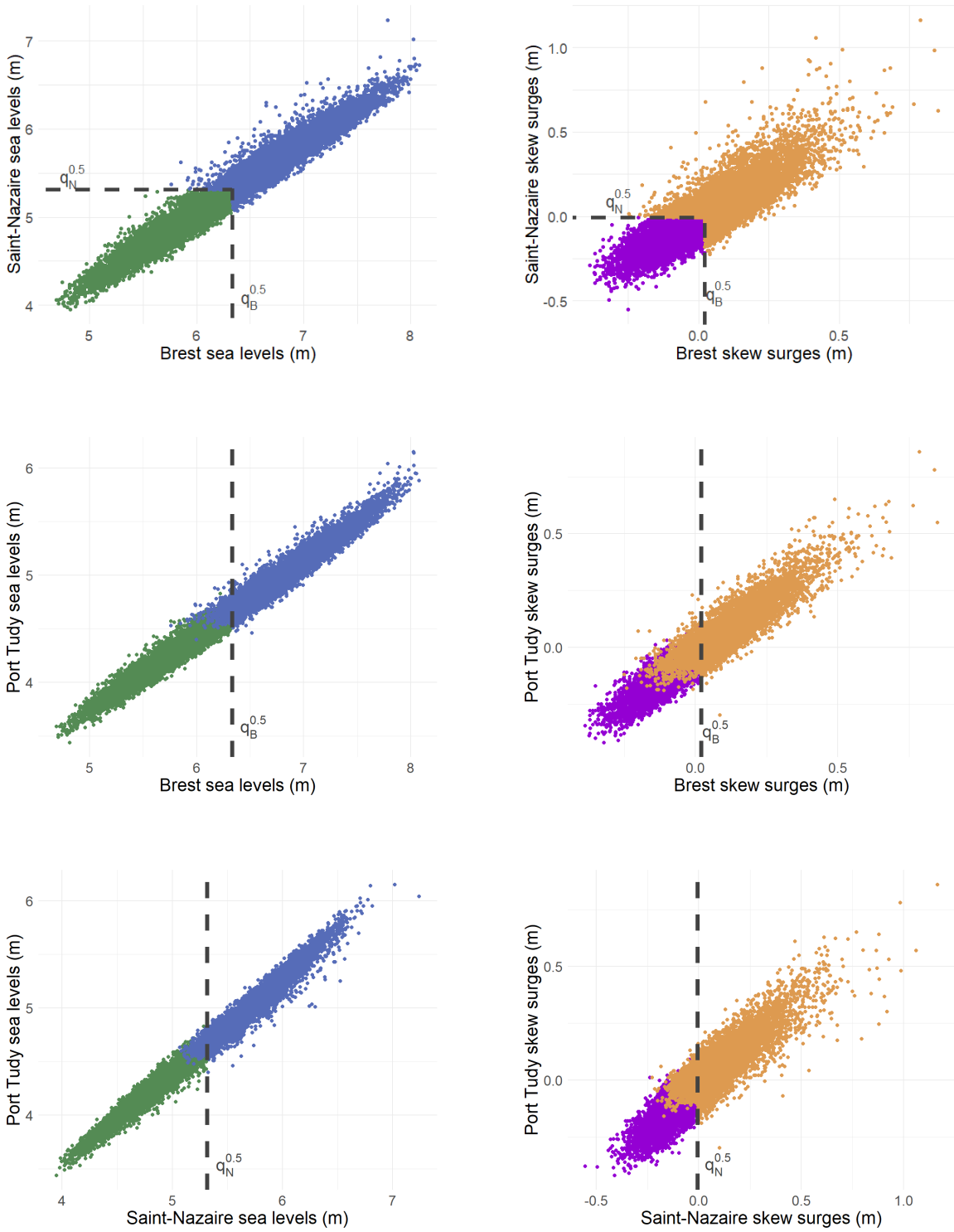


Figure 11: Scatter plots showing sea levels (left) and skew surges (right) at each station plotted against one another in the training set. Green and purple points represent the observations such that X_B and X_N are both below their empirical medians. Blue and orange points represent the observations such that X_B or X_N are above their empirical medians. The grey dotted lines represent the empirical medians.

C Density models

For the sake of completeness, this section provides detailed steps for constructing MGP densities along with the explicit formulas for the proposed densities used in Section 5.2.

C.1 MGP density construction

Theorem 5 in Rootzén et al. (2018) provides the theoretical foundation for constructing MGP densities from a variety of underlying density functions.

First, recall the decomposition (3.9) of a standard MGP random vector \mathbf{Z}'_∞ as defined in (3.8)

$$\mathbf{Z}'_\infty = E + \mathbf{T} - \max \mathbf{T},$$

where $E \in \mathbb{R}$ is a unit exponential random variable and \mathbf{T} is a random vector valued in \mathbb{R}^{d+1} , independent of E . Suppose that \mathbf{T} has a density f_T . Based on the above decomposition, \mathbf{Z}'_∞ has also a density h_T given by

$$h_T(\mathbf{z}) = \mathbb{1}\{\max(\mathbf{z}) > 0\} \exp(-\max(\mathbf{z})) \int_0^{+\infty} \frac{f_T(\mathbf{z} + \log t)}{t} dt.$$

Second, Theorem 5 in Rootzén et al. (2018) also introduces an alternative method to construct a standard MGP density. Let $\mathbf{U} \in \mathbb{R}^{d+1}$ a random vector such that $0 < \mathbb{E}[\exp(U_j)] < \infty$, for $1 \leq j \leq d+1$. Suppose \mathbf{U} has a density f_U . Then, from this density, an another standard MGP density is given by the following function

$$h_U(\mathbf{z}) = \frac{\mathbb{1}\{\max(\mathbf{z}) > 0\}}{\mathbb{E}[\exp(\max(\mathbf{U}))]} \int_0^{+\infty} f_U(\mathbf{z} + \log t) dt.$$

Both methods demonstrate how a standard MGP density can be systematically derived from various general density functions.

C.2 Density models

The explicit formulas for the density models used in the MGPRED procedure, namely with independent Gumbel components and with independent reverse exponential components, are gathered in this section.

C.2.1 Densities with independent Gumbel components

The density function of a Gumbel distribution with parameters $\alpha_j > 0, \beta_j \in \mathbb{R}$ expressed as

$$f_j(z_j) = \alpha \exp(-\alpha(z_j - \beta_j)) \exp\left(-\exp(-\alpha(z_j - \beta_j))\right).$$

Given this, the joint density function for the random vectors \mathbf{T} and \mathbf{U} is the product of the marginal densities

$$f(\mathbf{z}) = \prod_{j=1}^n f_j(z_j).$$

To simplify computations and avoid numerical approximations of integral quantities, we restrict the study to the case $\alpha_1 = \dots = \alpha_d = \alpha$. Under this simplification, the standard MGP density for the construction using \mathbf{T} is given by

$$h_T(\mathbf{z}) = \exp(-\max(\mathbf{z})) \alpha^{d-1} \frac{\Gamma(d) \prod_{j=1}^d \exp(-\alpha(z_j - \beta_j))}{\left(\sum_{j=1}^d \exp(-\alpha(z_j - \beta_j))\right)^d},$$

Similarly, the standard MGP density for the construction using \mathbf{U} is given by

$$h_U(\mathbf{z}) = \frac{\alpha^{d-1} \Gamma(d-1/\alpha)}{\Gamma(1-1/\alpha) \left(\sum_{j=1}^d \exp(\beta_j \alpha)\right)^{1/\alpha}} \frac{\prod_{j=1}^d \exp(-\alpha(z_j - \beta_j))}{\left(\sum_{j=1}^d \exp(-\alpha(z_j - \beta_j))\right)^{d-1/\alpha}}.$$

C.2.2 Densities with independent reverse exponential components

The density function of a reverse exponential distribution with parameters $\alpha_j > 0, \beta_j \in \mathbb{R}$ expressed as

$$f_j(z_j) = \alpha_j \exp(\alpha_j(z_j + \beta_j)),$$

for $z_j \in (-\infty, -\beta_j)$. Given this, the joint density function for the random vectors \mathbf{T} and \mathbf{U} is the product of the marginal densities

$$f(\mathbf{z}) = \prod_{j=1}^n f_j(z_j)$$

The standard MGP density for the construction using \mathbf{T} is then given by

$$h_T(\mathbf{z}) = \frac{\exp(-\max(\mathbf{z}) - \max(\mathbf{z} + \boldsymbol{\beta}) \sum_{j=1}^d \alpha_j)}{\sum_{j=1}^d \alpha_j} \prod_{j=1}^d \alpha_j \exp(\alpha_j(z_j + \beta_j)).$$

Similarly, the standard MGP density for the construction using \mathbf{U} is given by

$$h_U(\mathbf{z}) = \frac{\exp(-\max(\mathbf{z} + \boldsymbol{\beta})(\sum_{j=1}^d \alpha_j + 1))}{(1 + \sum_{j=1}^d \alpha_j) \mathbb{E}[\exp(\max(\mathbf{U}))]} \prod_{j=1}^d \alpha_j \exp(\alpha_j(z_j + \beta_j)),$$

D Additional studies

In this section, we present first the study using the sea levels at Port Tudy as output variable and then, the studies using Concarneau and Le Crouesty as output tide gauges.

D.1 Sea level study at Port Tudy

The training set comprises 8,271 observations ranging from 10-08-1966 to 31-12-1999 and the test set comprises 7,483 observations ranging from 01-01-2000 to 31-12-2023. Histogram plots with the corresponding fitted densities are shown in Figure 12. After thresholding, the final training set consists of 2,478 sea level exceedances, while final test set consists of 2,021 sea level exceedances.

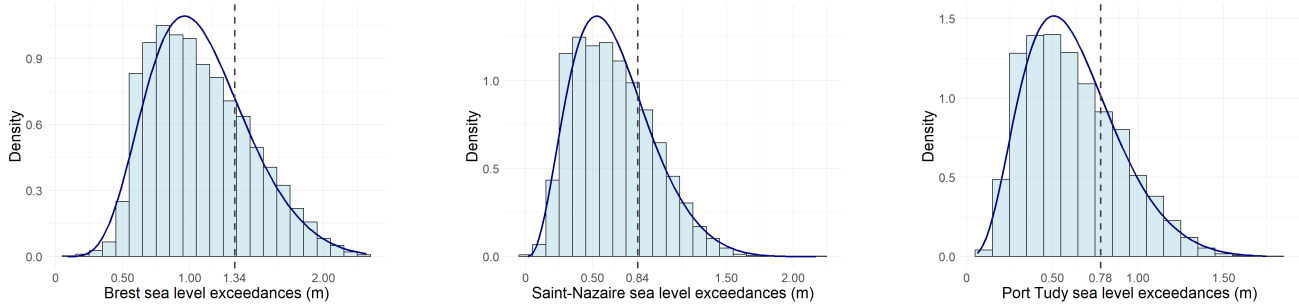


Figure 12: Histograms of sea level exceedances at the three stations Brest (left), Saint-Nazaire (middle) and Port Tudy (right), from 01/12/2000 to 31/12/2023. The darkblue curves represent the fitted EGP densities, with parameters specified in Table 1. The dotted vertical grey lines represent the smallest point above which each fitted density is convex, which represent the chosen marginal thresholds via Algorithm 1.

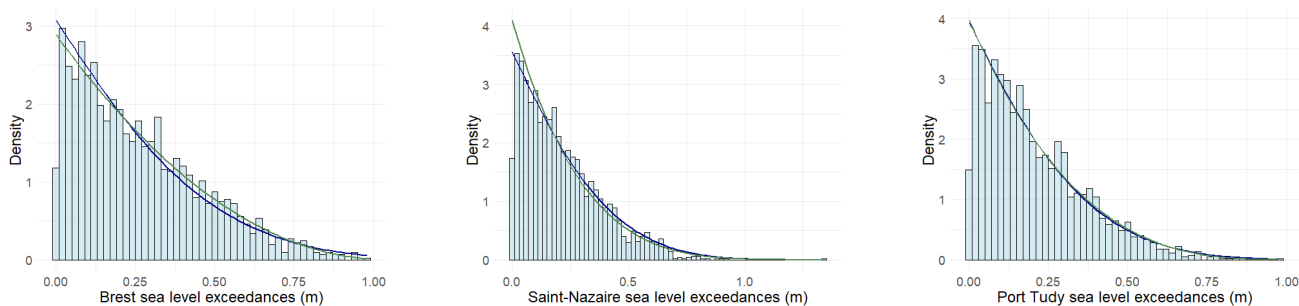


Figure 13: Histograms of sea level exceedances above the threshold specified in Table 3 at the three stations Brest (left), Saint-Nazaire (middle) and Port Tudy (right), from 01/12/2000 to 31/12/2023. The orange curves represent the fitted EGP densities above the thresholds, with parameters specified in Table 3. The purple curves represent the fitted GP densities.

Table 3: Point estimates of the parameters of the fitted EGP distribution for sea level exceedances at the three stations. The chosen thresholds, determined using via Algorithm 1, are shown in the t rows. The data used for inference are from the training set ranging from 01/12/2000 to 31/12/2023.

PARAMETERS/STATIONS	BREST	SAINT-NAZAIRE	PORT TUDY
σ	0.52	0.40	0.36
ξ	-0.18	-0.18	-0.17
κ	7.76	3.90	4.44
t	1.34	0.84	0.78

Table 4: RMSE*10²(SSE*10²) and MAE*10²(ASE*10²) of predicted sea level exceedances at Port Tudy station from the ROXANE procedure with RF regression (ROX RF), ROXANE procedure with OLS regression (ROX OLS) and MGPRED. Errors are measured on the test set covering the period from 10/08/1966 to 31/12/1999. Errors are computed for the entire test set (columns: RMSE and MSE) and for the subset of the test set comprising the most extreme observations w.r.t. the Port Tudy observations, *i.e.*, observations such that $Y_i \geq q_Y^{ext,0.5}$ (columns: RMSE_{ext} and MAE_{ext}).

TRAINING MODELS/ERRORS	RMSE	MAE	RMSE _{EXT}	MAE _{EXT}
ROX RF	8.1(0.3)	5.9(0.1)	7.7(0.4)	5.5(0.2)
ROX OLS	8.0(0.3)	5.9(0.1)	7.7(0.4)	5.5(0.2)
MGPRED	7.8(0.3)	5.7(0.1)	8.1(0.4)	5.8(0.2)

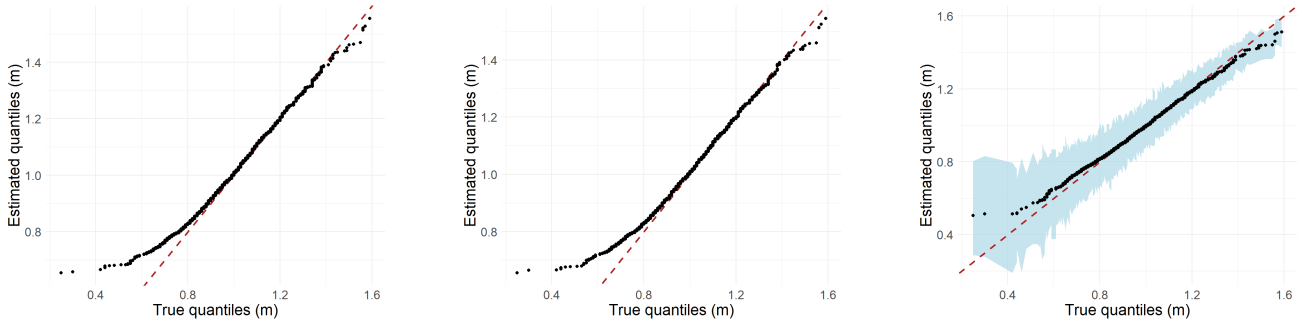


Figure 14: QQ-plots comparing observed sea level exceedances of the Port Tudy test set (x-axis), ranging from 10/08/1966 to 31/12/1999, to predicted data (y-axis) from the algorithms of Sections 4.2 and 4.3. The plots show results from the ROXANE procedure with RF regression (left), ROXANE procedure with OLS regression (middle), and MGPREd (right) with bootstrap 0.95 confidence bands (lightblue). The dotted red line represents the identity line $x = y$.

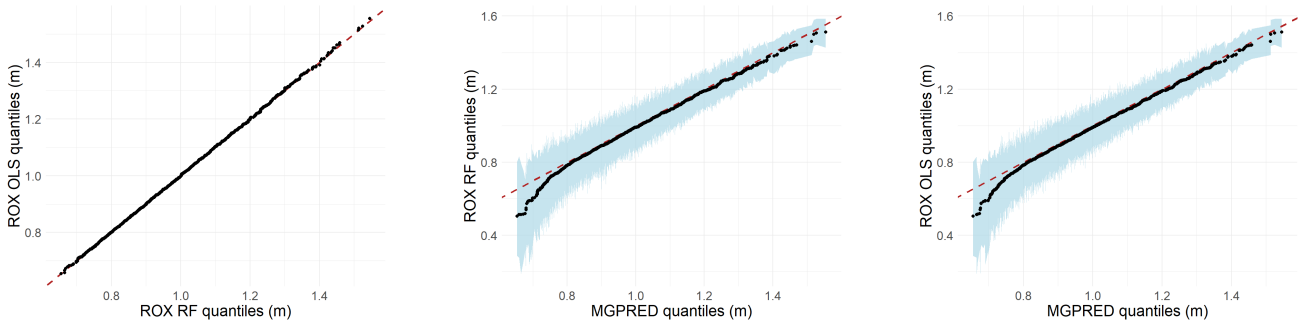


Figure 15: QQ-plots comparing predicted sea level exceedances of the Port Tudy test set, ranging from 10/08/1966 to 31/12/1999, from the algorithms of Sections 4.2 and 4.3: ROX RF *vs* ROX RF (left), MGPREd *vs* ROX RF (middle), and MGPREd *vs* ROX OLS (middle), with bootstrap 0.95 confidence bands (lightblue) from MGPREd. The dotted red line represents the identity line $x = y$.

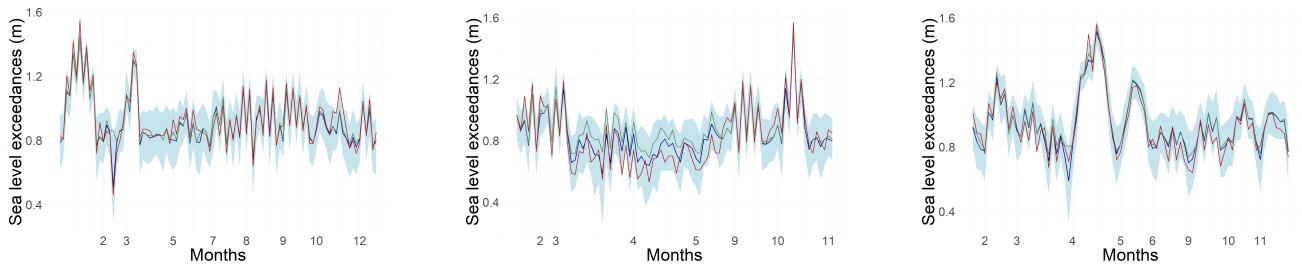


Figure 16: Predicted sea levels at Port Tudy station for the years 1996 (left), 1987 (middle), 1985 (right). These years are characterized by significant sea levels at the Port Tudy tide gauge. Red curves represent the true values on the test set; green curves represent the predicted values by the ROXANE procedure with OLS algorithm; blue curves represent the predicted values by MGPREd with bootstrap 0.95 confidence intervals (lightblue). The global 0.95-coverage probability is 0.93.

D.2 Concarneau study

Table 5: RMSE*10²(SSE*10²) and MAE*10²(ASE*10²) of predicted sea level and skew surge exceedances at Concarneau station from the ROXANE procedure with RF regression (ROX RF), ROXANE procedure with OLS regression (ROX OLS) and MGPRED. Errors are measured on the test set covering the period from 28/06/1999 to 31/12/2010. Errors are computed for the entire test set (columns: RMSE and MSE) and for the subset of the test set comprising the most extreme observations w.r.t. the Concarneau observations, *i.e.*, observations such that $Y_i \geq q_Y^{ext,0.5}$ (columns: RMSE_{EXT} and MAE_{EXT}).

TRAINING MODELS/ERRORS	RMSE	MAE	RMSE _{EXT}	MAE _{EXT}
SEA LEVELS: ROX RF	6.6(0.4)	4.7(0.2)	6.7(0.5)	5.0(0.2)
ROX OLS	6.2(0.4)	4.5(0.1)	6.4(0.4)	4.8(0.2)
MGPRED	6.3(0.3)	4.7(0.1)	7.1(0.5)	5.3(0.2)
SKEW SURGES: ROX RF	6.6(0.4)	4.9(0.1)	6.5(0.3)	5.2(0.2)
ROX OLS	6.6(0.4)	5.0(0.1)	6.4(0.3)	5.1(0.2)
MGPRED	6.4(0.2)	5.1(0.1)	7.0(0.3)	5.8(0.2)

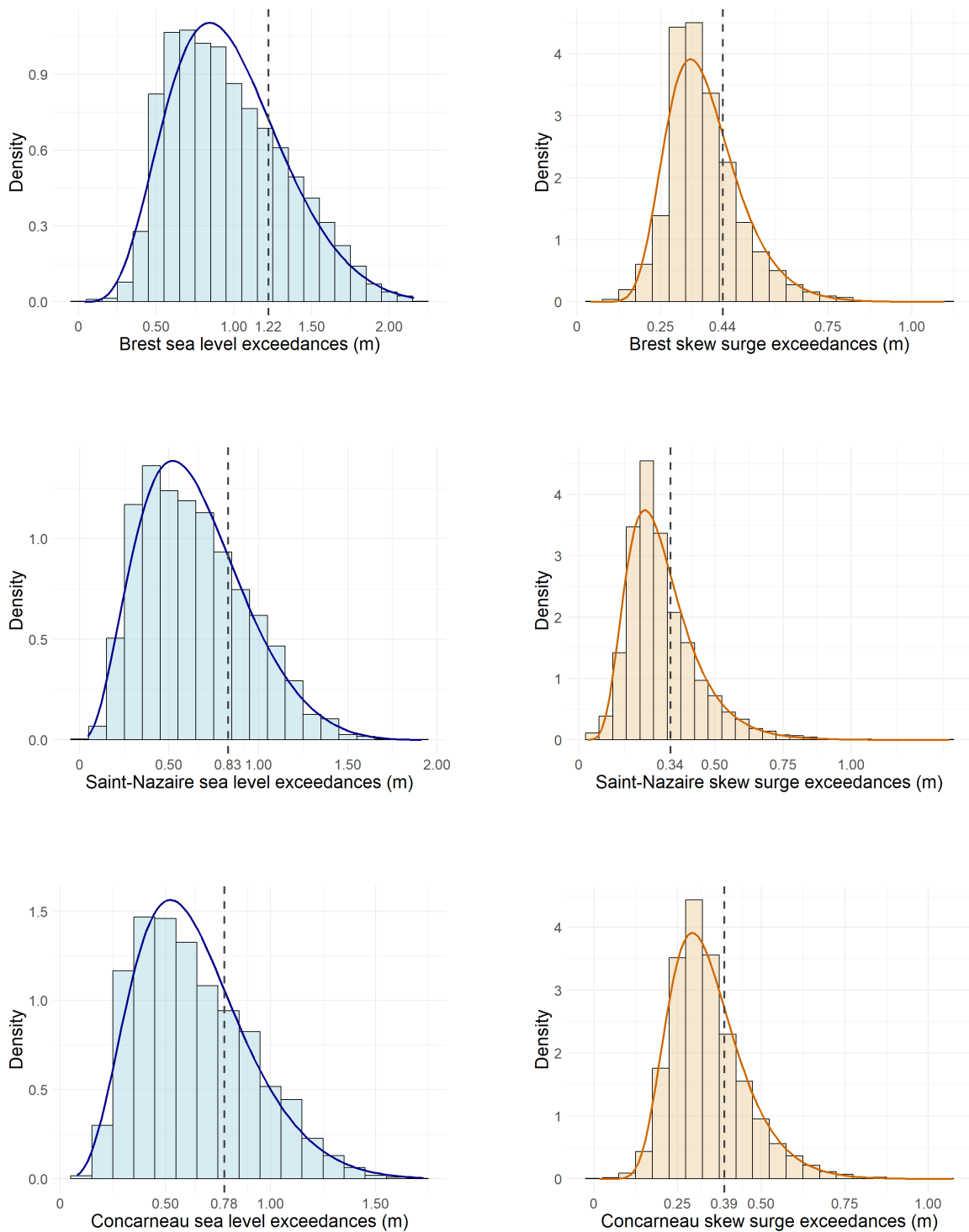


Figure 17: Histograms of sea level (right) and skew surge (right) exceedances at the three stations Brest (top row), Saint-Nazaire (middle row) and Concarneau (bottom row), from 28/06/1999 to 31/12/2010. The darkblue and darkorange curves represent the fitted EGP densities. The dotted vertical grey lines represent the smallest point above which each fitted density is convex, which represent the chosen marginal thresholds via Algorithm 1.

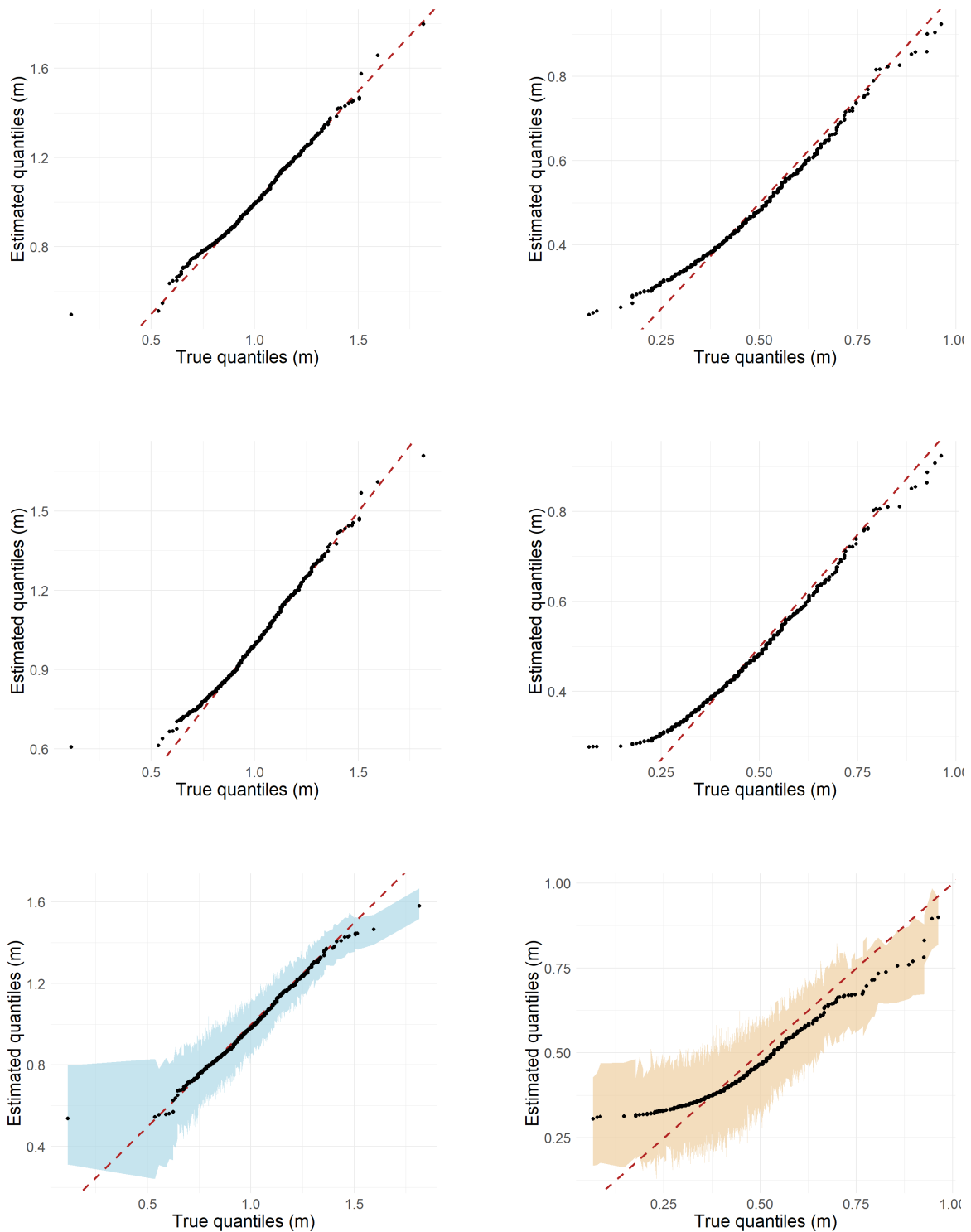


Figure 18: QQ-plots comparing observed sea level (left) and skew surge (right) exceedances of the Concarneau test set (x-axis), ranging from 28/06/1999 to 31/12/2010, to predicted data (y-axis) from the algorithms of Sections 4.2 and 4.3. The plots show results from the ROXANE procedure with RF regression (top row), ROXANE procedure with OLS regression (middle row), and MGPREP (bottom row) with bootstrap 0.95 confidence bands (lightblue and lightorange). The dotted red line represents the identity line $x = y$. The global 0.95-coverage probability associated with MGPREP is 0.95 for sea levels and 0.96 for skew surges.

D.3 Le Crouesty study

Table 6: RMSE*10²(SSE*10²) and MAE*10²(ASE*10²) of predicted sea level and skew surge exceedances at Le Crouesty station from the ROXANE procedure with RF regression (ROX RF), ROXANE procedure with OLS regression (ROX OLS) and MGPRED. Errors are measured on the test set covering the period from 14/03/1996 to 31/12/2014. Errors are computed for the entire test set (columns: RMSE and MSE) and for the subset of the test set comprising the most extreme observations w.r.t. the Le Crouesty observations, *i.e.*, observations such that $Y_i \geq q_Y^{ext,0.5}$ (columns: RMSE_{ext} and MAE_{ext}).

TRAINING MODELS/ERRORS	RMSE	MAE	RMSE _{EXT}	MAE _{EXT}
SEA LEVELS: ROX RF	5.9(0.3)	4.4(0.1)	5.6(0.4)	4.3(0.2)
ROX OLS	5.9(0.3)	4.3(0.1)	5.6(0.4)	4.3(0.2)
MGPRED	6.5(0.4)	4.8(0.1)	6.8(0.6)	4.9(0.2)
SKREW SURGES: ROX RF	5.9(0.3)	4.4(0.1)	5.8(0.5)	4.1(0.2)
ROX OLS	5.8(0.3)	4.3(0.1)	5.6(0.5)	4.1(0.2)
MGPRED	5.6(0.3)	4.2(0.1)	6.0(0.4)	4.6(0.2)

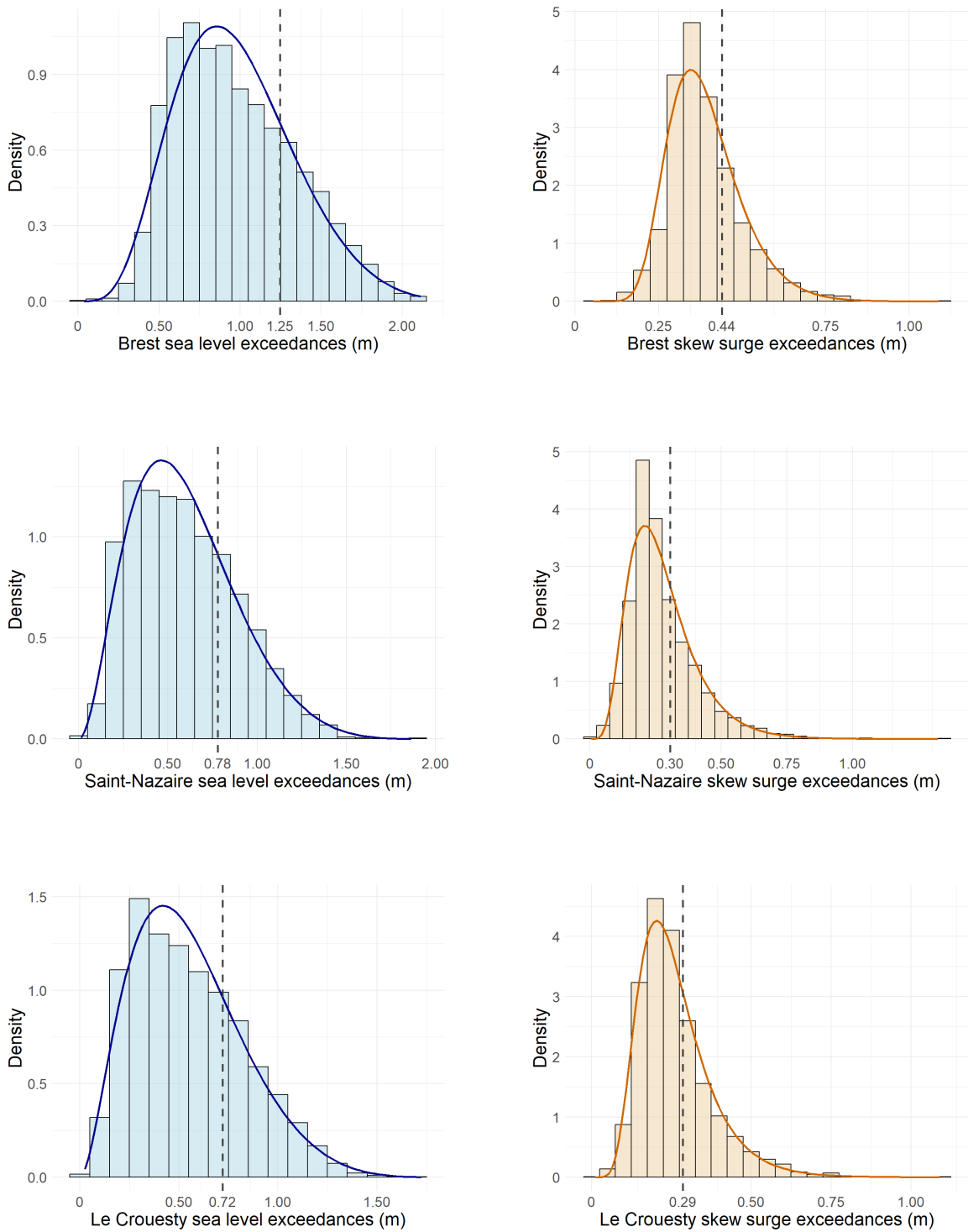


Figure 19: Histograms of sea level (left) and skew surge (right) exceedances at the three stations Brest (top row), Saint-Nazaire (middle row) and Le Croesty (bottom row), from 14/03/1996 to 31/12/2014. The darkblue and darkorange curves represent the fitted EGP densities. The dotted vertical grey lines represent the smallest point above which each fitted density is convex, which represent the chosen marginal thresholds via Algorithm 1.

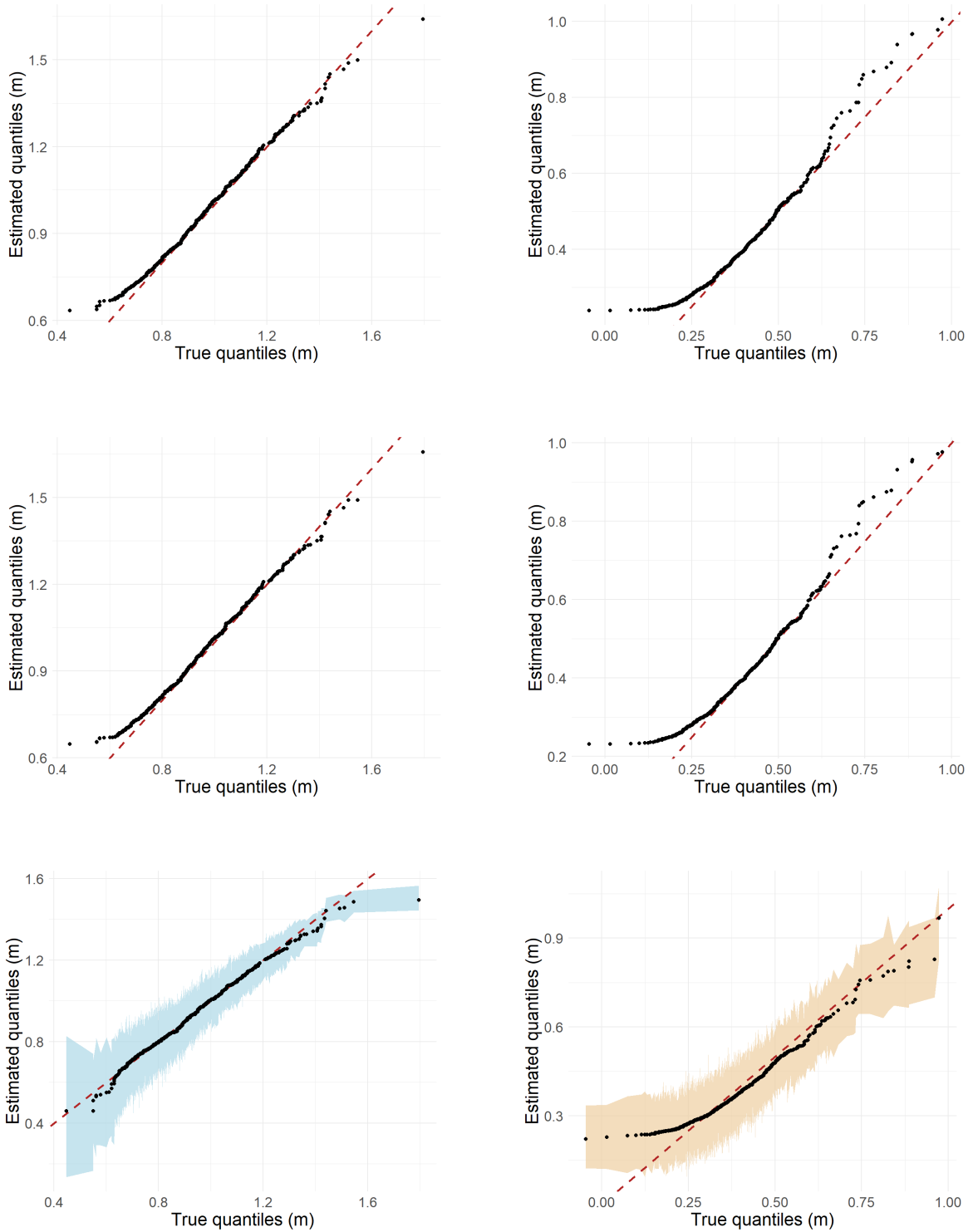


Figure 20: QQ-plots comparing observed sea level (left) and skew surge (right) exceedances of the Le Crouesty test set (x-axis), ranging from 14/03/1996 to 31/12/2014, to predicted data (y-axis) from the algorithms of Sections 4.2 and 4.3. The plots show results from the ROXANE procedure with RF regression (top row), ROXANE procedure with OLS regression (middle row), and MGPREP (bottom row) with bootstrap 0.95 confidence bands (lightblue and lightorange). The dotted red line represents the identity line $x = y$. The global 0.95-coverage probability associated with MGPREP is 0.97 for sea levels and 0.97 for skew surges.